iScience

CellPress
OPEN ACCESS

Article

KMT2D suppresses Sonic hedgehog-driven medulloblastoma progression and metastasis

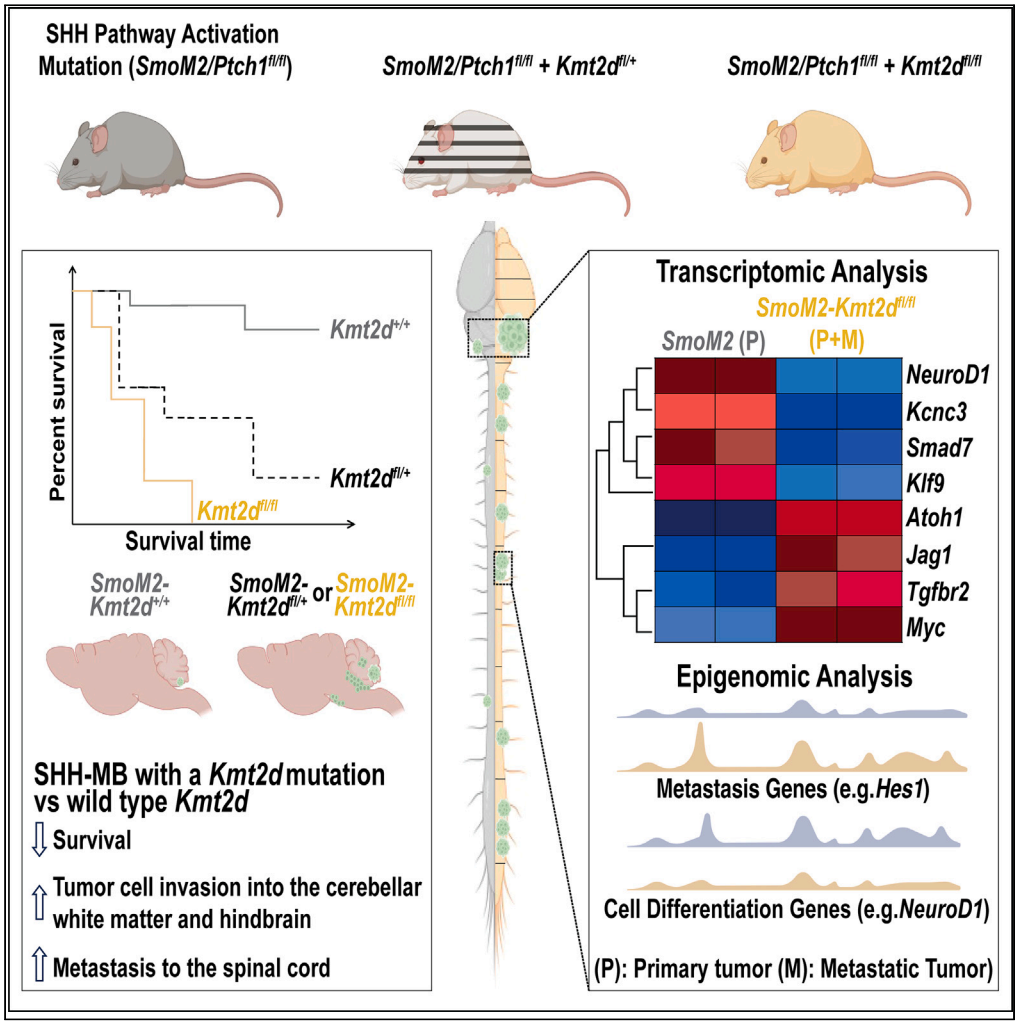

Reeti Mayur Sanghrajka, Richard Koche, Hector Medrano, ..., N. Sumru Bayin, Kai Ge, Alexandra L. Joyner

joynera@mskcc.org

Highlights

Heterozygous and homozygous loss of *Kmt2d* decreases survival in SHH-MB

Kmt2d mutations increase spinal cord metastasis in two mouse models of SHH-MB

Tumors lacking *Kmt2d* have decreased expression of neural differentiation genes

Tumors lacking *Kmt2d* upregulate stem cell maintenance and metastasis genes

Sanghrajka et al., iScience *26*, 107831
October 20, 2023
https://doi.org/10.1016/j.isci.2023.107831

iScience

CellPress
OPEN ACCESS

Article

KMT2D suppresses Sonic hedgehog-driven medulloblastoma progression and metastasis

Reeti Mayur Sanghrajka,[1,2] Richard Koche,[3] Hector Medrano,[1] Salsabiel El Nagar,[1] Daniel N. Stephen,[1] Zhimin Lao,[1] N. Sumru Bayin,[1,5] Kai Ge,[4] and Alexandra L. Joyner[1,2,6,*]

SUMMARY

The major cause of treatment failure and mortality among medulloblastoma patients is metastasis intracranially or along the spinal cord. The molecular mechanisms driving tumor metastasis in Sonic hedgehog-driven medulloblastoma (SHH-MB) patients, however, remain largely unknown. In this study we define a tumor suppressive role of *KMT2D* (*MLL2*), a gene frequently mutated in the most metastatic β-subtype. Strikingly, genetic mouse models of SHH-MB demonstrate that heterozygous loss of *Kmt2d* in conjunction with activation of the SHH pathway causes highly penetrant disease with decreased survival, increased hindbrain invasion and spinal cord metastasis. Loss of *Kmt2d* attenuates neural differentiation and shifts the transcriptional/chromatin landscape of primary and metastatic tumors toward a decrease in differentiation genes and tumor suppressors and an increase in genes/pathways implicated in advanced stage cancer and metastasis (TGFβ, Notch, *Atoh1*, *Sox2*, and *Myc*). Thus, secondary heterozygous *KMT2D* mutations likely have prognostic value for identifying SHH-MB patients prone to develop metastasis.

INTRODUCTION

The cerebellar tumor medulloblastoma (MB) is the most common malignant pediatric brain tumor, and encompasses 4 major disease subgroups: Wingless-related integration site (WNT), Sonic hedgehog (SHH), group 3, and group 4.[1–5] Metastasis is the major cause of morbidity and mortality among MB patients and occurs most commonly intracranially or along the spinal cord, as a result of hematogenous or leptomeningeal dissemination (LMD).[6–12] SHH-MB accounts for ~30% of all MB cases and has an intermediate prognosis with a metastasis rate of 15–35%.[4,13–18] Of the four subgroups of MB, mouse models of SHH-MB are the most advanced and have been used to implicate over-expression of several genes including *Atoh1* in promoting metastasis with LMD throughout the brain and spinal cord.[8,11,19,20] However, the human correlates of the mutations in SHH-MB disease are not clear. Given the lifelong neurological sequalae suffered by patients that survive surgery and treatments for SHH-MB, identification of prognostic markers and potential druggable targets are essential to improve survival and quality of life, especially for treating metastatic disease.

SHH-MB arises from granule cell precursors (GCPs) that cover the surface of the cerebellum[21–24] during the third trimester and first year of life[25] and tumors form preferentially in the lateral cerebellar hemispheres.[26–29] GCPs are dependent on SHH-signaling and ATOH1 to maintain a proliferative progenitor state.[30–32] Most patients within this subgroup harbor mutations at one of four genes that lead to constitutive activation of the SHH pathway: loss-of-function mutations in *PTCH1* or *SUFU*, gain-of-function mutations in *SMO* and *TP53* mutations associated with amplification of *GLI2* or *MYCN*.[33–36] SHH-MB has been deconstructed into several subtypes based on patient demographics, genomic and epigenomic landscapes, tumor histology, metastatic status, and clinical outcomes.[37–41] A widely accepted subtyping categorizes SHH-MB into 4 subtypes: α, β, γ, and δ.[38,41] The β subtype occurs most frequently in infants and has the highest incidence of metastasis (30–35%) and the worst 5-year survival rate (65–70%).[34,41,42] Mutations in *PTCH1* and *SUFU* that activate SHH signaling are prevalent in the β-subtype of SHH-MB.[34,41,42] In addition, recurrent mutations in *KMT2D* are preferentially seen in this subtype of SHH-MB;[34,41,42] however, the consequences of such mutations on disease progression and metastasis have not been explored in animal models.

Somatic mono-allelic mutations in *KMT2D* (also known as *MLL2* in humans and *Mll4* in mouse) that are predicted to result in a truncated protein are seen in 8–15% of SHH-MB patients.[34,36,42–46] KMT2D is a SET-domain containing histone-lysine N-methyltransferase that mono-,

[1]Developmental Biology Program, Sloan Kettering Institute of Memorial Sloan Kettering Cancer Center, New York, NY, USA
[2]Biochemistry, Cell and Molecular Biology Program, Weill Cornell Graduate School of Medical Sciences, New York, NY, USA
[3]Center for Epigenetics Research, Memorial Sloan Kettering Cancer Center, New York, NY, USA
[4]Adipocyte Biology and Gene Regulation Section, National Institute of Diabetes and Digestive and Kidney Diseases, National Institutes of Health (NIH), Bethesda, MD, USA
[5]Present address: Wellcome Trust/Cancer Research UK Gurdon Institute, and Department of Physiology, Development and Neuroscience, Cambridge University, Cambridge, UK
[6]Lead contact
*Correspondence: joynera@mskcc.org
https://doi.org/10.1016/j.isci.2023.107831

di-, or tri-methylates (me1, me2, me3) lysine 4 on histone H3 (H3K4) preferentially at gene enhancers or promoters to generate a mark associated with active transcription or a poised bivalent state of genes.[47–50] The roles described for *KMT2D* during development and tumor progression are context-dependent,[50,51] and little is known about its role in medulloblastoma. Mice with a nervous system-specific floxed conditional mutation in *Kmt2d* (exons 16–19; *Nestin-Cre/+; Kmt2d*$^{f/f}$) were reported to be viable and have a morphologically normal cerebellum at one month of age, although granule neurons and Purkinje cells appeared to lack some mature marker proteins.[50] Nonetheless, 35% of male homozygous mutants went on to develop MB-like tumor growths in the cerebellum by 7 months. Based on transcriptional profiling of three lesions, the tumors were described to best resemble group 3 MB.[50] This result indicates that *KMT2D* is a tumor suppressor in MB. However, a role in SHH-MB or in metastasis has not been addressed.

Given the prevalence of *KMT2D* mutations in SHH-MBs and enrichment in the β-subtype (12–30% in Garcia-Lopez et al. and Skowron et al.),[34,42] we tested the impact of heterozygous and homozygous *Kmt2d* mutations in the context of mouse models of SHH-MB. Using two sporadic genetic models, *Smo* activation (*SmoM2*) and *Ptch1* loss (*Ptch1*$^{fl/fl}$) combined with N- and C-terminal floxed truncating alleles of *Kmt2d* we show that heterozygous or homozygous loss of *Kmt2d* in rare postnatal GCPs greatly accelerates SHH-MB tumorigenesis and penetrance compared to mice with only a SHH pathway activating mutation. Furthermore, loss of *Kmt2d* drives tumor cell invasion into the surrounding brain. Most notably, heterozygous loss of *Kmt2d* is sufficient to drive fully penetrant leptomeningeal metastasis to the spinal cord, a hallmark of advanced stage disease. Transcriptomic and chromatin analyses revealed major differences between primary tumors with intact or mutant *Kmt2d* in the context of SmoM2 expression but the metastatic landscape of *Kmt2d* mutant cells is similar to primary *Kmt2d* mutant tumors. Of likely significance, tumors lacking *Kmt2d* have upregulation of genes involved in pathways implicated in stem cell maintenance and cellular processes associated with tumor metastasis including cell migration and epithelial to mesenchymal transition (EMT). The data indicate the mechanism involves KMT2D normally augmenting expression of neural differentiation genes and repressors of Notch and TGF signaling. Our findings thus reveal that *Kmt2d* is a potent suppressor of SHH-MB tumor growth, invasion, and metastasis, and when reduced changes the transcriptional/chromatin landscape of SHH-MB into an aggressive disease increasing oncogenic programs including TGFβ,[52] Notch,[50,53] MYC,[54,55] ATOH1,[11] and SOX2/9.[56–60]

RESULTS

KMT2D mutations are prevalent in SHH-MB and co-occur with mutations that activate SHH signaling

To gain insight into the significance of *KMT2D* mutations in SHH-MB, we determined the frequency of mutations in *KMT2D* and its homolog *KMT2C*, as well as mutations that activate SHH-signaling in 127 patient samples considered to be SHH-MB[36] using the cBioPortal.[61,62] Like previous studies, we found that *KMT2D* is mutated in ∼14% of the samples (Figure 1A), whereas *KMT2C* mutations are less prevalent (∼6%) (Figure 1A). Furthermore, in 66% of the samples the mutations in *KMT2D* occur in conjunction with mutations in genes that lead to activation of the SHH pathway (*SMO*, *PTCH1*, *SUFU*, and *TP53*) (Figure 1A). Thus, *KMT2D* mutations are recurrent in SHH-MB and frequently co-occur with SHH pathway activating mutations, indicating *KMT2D* mutations are secondary mutations that might impact tumor progression.

N-terminal and C-terminal mutations in *Kmt2d* transiently disrupt cerebellum development

Before testing whether mutations in *Kmt2d* impact disease severity in sporadic mouse models of SHH-MB with low penetrance, we revisited whether *Kmt2d* alone plays a role in cerebellum development. Since several mouse conditional mutant alleles of *Kmt2d* have been generated, we first tested the consequences of conditional deletion of *Kmt2d* using the *Nestin-Cre* transgene utilized previously by Dhar et al. (2018) to delete the same N-terminal exons (16–19) in the brain (floxed allele referred to as *Nf*;[63] [Figure 1B]) or C-terminal exons 50–51 (floxed allele referred to as *Cf*;[64] [Figure 1C]). Surprisingly, we found that both *Nes-Cre/+; Kmt2d*$^{Nf/Nf}$ and *Nes-Cre/+; Kmt2d*$^{Cf/Cf}$ conditional mutants do not survive past birth (n > 85 and n > 50 animals, respectively examined from crosses of *Nes-Cre/+; Kmt2d*$^{f/+}$ X *Kmt2d*$^{f/f}$ mice). Embryonic day (E) 18 brains from both homozygous mutants had similar sized cerebella to littermate controls but surface folding of the cerebella was significantly reduced in both mutants suggesting a decrease in expansion of the GCPs in the external granule layer (EGL)[65] (Figures 1D–1I). Consistent with this, the area of the EGL was reduced in E18.5 *Nes-Cre/+; Kmt2d*$^{Cf/Cf}$ mutants compared to controls (Figure S1A) and the proportion of the EGL made up of differentiating cells was reduced (Figure S1B), although the proliferation rate of GCPs was not reduced at E18.5 in *Nes-Cre/+; Kmt2d*$^{Cf/Cf}$ mutants (Figure S1C). These results indicates *Kmt2d* normally promotes differentiation of GCPs.

As a means to circumvent the lethality seen in our *Nes-Cre* conditional mutants, we deleted *Kmt2d* in three lineages of the embryonic cerebellum which together comprise all the cell types in the cerebellum: (1) the rhombic lip excitatory neuron lineage (including GCPs) using an *Atoh1-Cre* transgene,[66] (2) the ventricular zone inhibitory neuron lineage (Purkinje cells and interneurons) using a *Ptf1a*^{Cre} allele,[67] and (3) the ventricular zone-derived Bergmann glia, astrocytes, late born interneurons and rhombic-lip-derived GCPs and unipolar brush cells using a *hGFAP-Cre* transgene.[68] We found that the *Atoh1-Cre; Kmt2d*$^{Cf/Cf}$, *Ptf1a*$^{Cre/+}$; *Ktm2d*$^{Cf/Cf}$, and *hGFAP-Cre; Ktm2d*$^{Cf/Cf}$ conditional mutants survived to adulthood, and moreover when aged to >P200 none had cerebellar tumors or major foliation or size defects (n = 25, 25, and 15, respectively; Figures 1J–1M). Furthermore, in P30 mutants, granule cell and Purkinje cell marker protein expression (NeuN and Calbindin, respectively) appeared normal compared to littermate controls (n = 3; Figures S1D–S1E′). Thus, in our mouse genetic background nervous system homozygous conditional mutation of *Kmt2d* using two distinct alleles of *Kmt2d* cause similar cerebellar developmental defects at E18.5 and lethality at birth, whereas lineage-specific *Ktm2d*$^{Cf/Cf}$ homozygous deletion alone does not result in lethality or lead to cerebellar tumor formation.

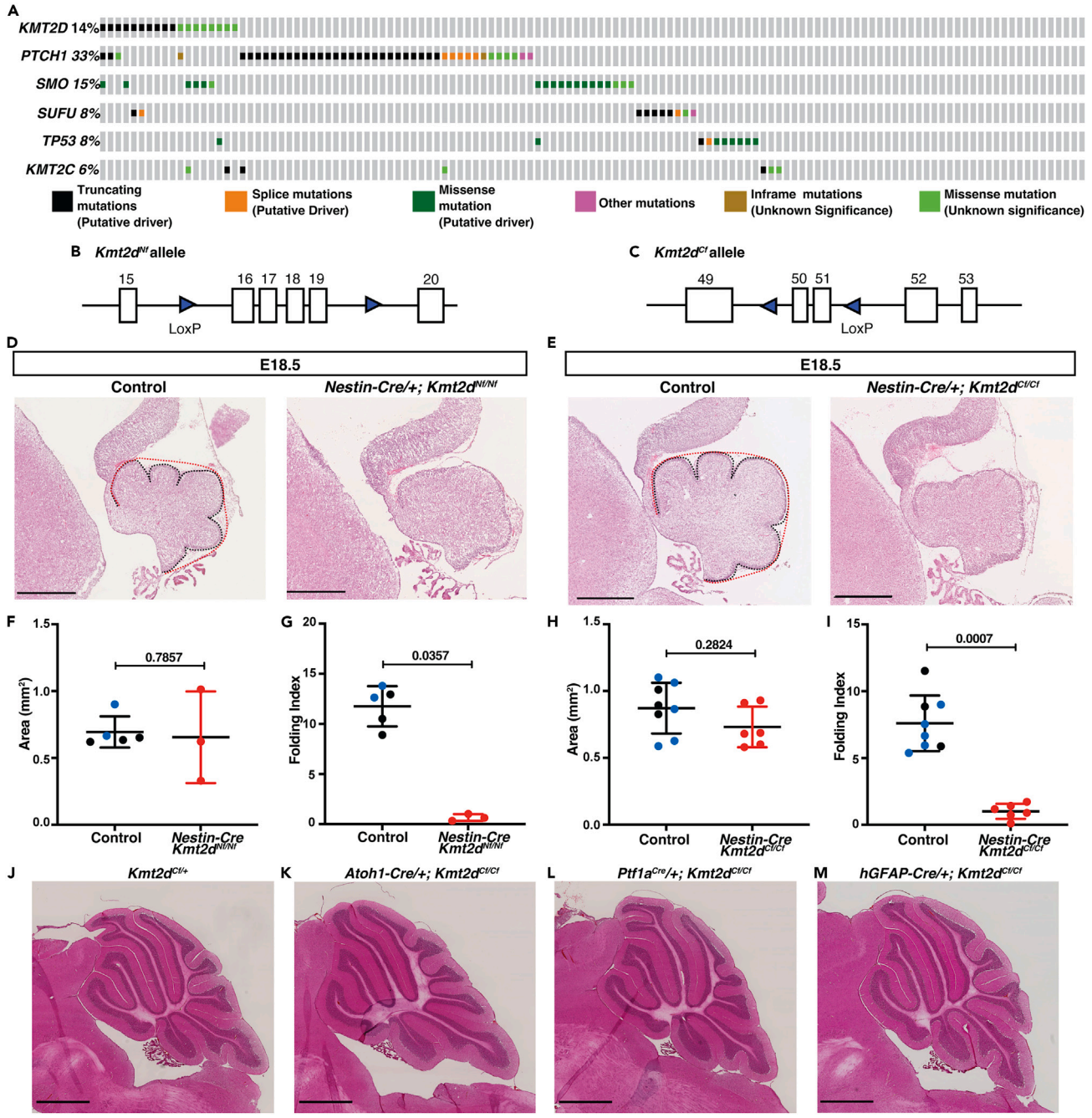

Figure 1. Two mutations in *Kmt2d* delay early cerebellum development but *Kmt2d* loss does not drive SHH-MB tumorigenesis

(A) An oncoprint of 127 patient samples considered to be SHH-MB (Kool et al., 2014) using the cBioPortal (Cerami et al., 2012; Gao et al., 2013a) showing the frequency of mutations in *KMT2C/D* and genes that activate the SHH pathway.

(B) Schematic of mouse *Kmt2d*^{Nf} floxed allele with *loxP* sites surrounding exons 16–19.[63]

(C) Schematic of mouse *Kmt2d*^{Cf} floxed allele with *loxP* sites surrounding exons 50 and 51.[64]

(D and E) H&E-stained mid-sagittal sections from E18.5 animals of the indicated genotypes with the EGL length in black and convex cerebellar length in red. Scale bars: 500 μm.

(F–I) Quantification at E18.5 of the cerebellar area (mm^2) (F and H) and Folding Index ((1-[convex length/EGl length]) x 100) in control (*Kmt2d*$^{Nf/+}$ and *Kmt2d*$^{Nf/Nf}$ or *Kmt2d*$^{Cf/+}$ and *Kmt2d*$^{Cf/Cf}$ embryos (black dots) or *Nes-Cre/+; Kmt2d*$^{Nf/+}$ or *Nes-Cre/+; Kmt2d*$^{Cf/+}$ (blue dots)) and conditional mutants (red dots) (G and I).

(J–M) Images of H&E-stained mid-sagittal sections from a control and *Kmt2d*$^{Cf/Cf}$ conditional mutants using the three *Cre* drivers at adult stages (P250-P300). Scale bars: 1 mm. Statistical significance was determined using an unpaired t-test. Error bars: SD. Also see Figure S1.

Secondary loss-of-function mutations in *Kmt2d* greatly increase SHH-MB tumor penetrance

We next tested whether loss of *Kmt2d* in two sporadic mouse models of SHH-MB with low penetrance enhance tumor formation. To closely model human SHH-MBs we used a Flp-inducible eGFP-Cre approach (MASTR: mosaic analysis with spatial and temporal control of recombination) in which *Atoh1-FlpoER* and tamoxifen induces simultaneous expression of *SmoM2* or deletion of both *Ptch1* alleles along with a heterozygous or homozygous deletion of *Kmt2d* in ~10,000 scattered GCPs at P2 (Figures 2A and 2B).[29,69] Strikingly, with the *SmoM2* model and C-terminal exon deletion of *Kmt2d*, we found that compared to control animals with intact *Kmt2d* (*Atoh1-FlpoER/+; R26*$^{MASTR/SmoM2}$ called *SmoM2*; n = 25), *Atoh1-FlpoER/+; R26*$^{MASTR/SmoM2}$*; Kmt2d*$^{Cf/+}$ (*SmoM2-Kmt2d*$^{Cf/+}$; n = 31) and *Atoh1-FlpoER/+; R26*$^{MASTR/SmoM2}$*; Kmt2d*$^{Cf/Cf}$ (*SmoM2-Kmt2d*$^{Cf/Cf}$; n = 38) mice had significantly different survival curves (Figure 2C). Whereas only 56% of *SmoM2* animals showed signs of tumor burden by P150, 87% of *SmoM2-Kmt2d*$^{Cf/+}$ and 100% of *SmoM2-Kmt2d*$^{Cf/Cf}$ did. We similarly found that a heterozygous or homozygous deletion of N-terminal exons of *Kmt2d* in the *SmoM2* model (*SmoM2-Kmt2d*$^{Nf/+}$ or *SmoM2-Kmt2d*$^{Nf/Nf}$, respectively) resulted in significantly different survival curves compared to *SmoM2* (Figure 2D). Penetrance by P150 was increased from 54% in *SmoM2* (n = 13) to 95% in *SmoM2-Kmt2d*$^{Nf/+}$ (n = 17) and 100% in *SmoM2-Kmt2d*$^{Nf/Nf}$ (n = 7) animals (Figure 2D). Since SHH-MB tumor biology is influenced by the type of mutation that activates SHH signaling,[29,36,42] we tested whether the *Cf* mutation in *Kmt2d* in a *Ptch1* model accelerates SHH-MB tumorigenesis. Indeed, *Ptch1-Kmt2d*$^{Cf/+}$ (*Atoh1-FlpoER/+; R26*$^{MASTR/+}$*; Ptch1*$^{f/f}$*; Kmt2d*$^{Cf/+}$; n = 19) and *Ptch1-Kmt2d*$^{Cf/Cf}$ (*Atoh1-FlpoER/+; R26*$^{MASTR/+}$*; Ptch1*$^{f/f}$*; Kmt2d*$^{Cf/Cf}$; n = 14) animals had significantly altered survival curves compared to *Ptch1* (*Atoh1-FlpoER/+; R26*$^{MASTR/+}$*; Ptch1*$^{f/f}$) (n = 41) (Figure 2E), with an increase in tumor penetrance by P200 from 27% in *Ptch1* mutants to 71% in *Kmt2d* heterozygotes and 93% in homozygotes. Of note, mutations in *Kmt2d* did not alter tumor histology—all genotypes had tumors with classic histology (Figures 2F–2N).

To confirm that *Kmt2d* was effectively deleted in homozygous mutant tumor cells and determine if a wild type (WT) allele was present in heterozygotes, we performed bulk RNA-sequencing (RNA-seq) of GFP+ tumor cells isolated by fluorescent activated cell sorting (FACS) from *SmoM2*, *SmoM2-Kmt2d*$^{Cf/+}$, and *SmoM2-Kmt2d*$^{Cf/Cf}$ animals (see details in the following; Table S1). Analysis of RNA-seq data confirmed a decrease in read counts for exons 50 and 51 in *SmoM2-Kmt2d*$^{Cf/+}$ animals compared to other exons and compared to *SmoM2* animals, and an absence of sequence reads for exons 50 and 51 in *SmoM2-Kmt2d*$^{Cf/Cf}$ animals (Figure 2O). To test the consequences of loss of *Kmt2d* on chromatin modification, we performed western blot analysis of whole tumor protein for H3K4me1 and H3K4me3 from end stage animals. The results showed a significant decrease in H3K4me1 and H3K4me3 in *SmoM2-Kmt2d*$^{Cfl/Cf}$ tumors compared to *SmoM2* and significant decrease in H3K4me3 in *SmoM2-Kmt2d*$^{Cf/+}$ animals (Figures S2A–S2C). Taken together, the survival data and molecular results demonstrate that KMT2D has a tumor suppressive role in SHH-MB. Furthermore, in *SmoM2-Kmt2d*$^{Cf/+}$ mice the decreased survival is due to haploinsufficiency, not loss of heterozygosity during tumor progression.

The pro-tumorigenic effect of loss of *Kmt2d* can be seen at P21

To assess how early the pro-tumorigenic effects of *Kmt2d* loss are initiated, tumor histology was analyzed at early stages of tumor development (P12 and P21) using the *SmoM2-Kmt2d*^{Cf} model. GFP staining of mutant cells on sagittal cerebellar hemisphere sections at P12 revealed the EGL was composed almost entirely of mutant GCPs in *SmoM2*, *SmoM2-Kmt2d*$^{Cf/+}$ and *SmoM2-Kmt2d*$^{Cf/Cf}$ animals, with no statistically significant differences in the percentage of the cerebellum that contains the EGL in animals with or without *Kmt2d* in the hemispheres or the vermis (Figures 3A–3E). Quantification of the density of dying cells (#TUNEL+ particles per EGL area) (Figures 3F–3I) and the proliferation rate (#EdU+ cells per EGL area) (Figures 3J–3M) in the thickened EGL in the posterior hemispheres also detected no significant difference in either measurement at P12. Thus, loss of *Kmt2d* at P2 in GCPs with co-activation of SHH signaling does not lead to an immediate increase in the number of GCPs. At P21, however, when no EGL is present in normal mice, there was a significant increase in the EGL/lesion areas in the hemispheres and vermis of *SmoM2-Kmt2d*$^{Cf/+}$ and *SmoM2-Kmt2d*$^{Cf/Cf}$ mice compared to in *SmoM2* mice (Figures 3N–3R). Thus, the increase in tumor progression seen after loss of *Kmt2d* in SHH-MB tumors can be seen by P21, a preneoplastic stage of tumorigenesis.

Loss of *Kmt2d* in SHH-MB leads to reduced expression of neural differentiation genes and repressors of Notch- and TGFβ-signaling and increased expression of genes associated with progenitor behaviors

To address the molecular mechanisms by which loss of *Kmt2d* promotes SHH-MB tumor progression, we compared the transcriptome and chromatin accessibility profiles of *SmoM2*, *SmoM2-Kmt2d*$^{Cf/+}$, and *SmoM2-Kmt2d*$^{Cf/Cf}$ primary tumors using bulk RNA-seq and ATAC-seq (Figure 4A; Table S1). The primary tumors were dissected from the brain and tumor cells were enriched for by isolation of GFP+ cells by FACS. Hierarchical clustering of bulk RNA-seq data ($p <= 0.05$; *fold change [FC] >= 1.5*) demonstrated that *SmoM2* tumors clustered separately from *SmoM2-Kmt2d*$^{Cf/Cf}$ and *SmoM2-Kmt2d*$^{Cf/+}$ tumors (Figure S3A; Table S2). Furthermore, *SmoM2-Kmt2d*$^{Cf/+}$ tumor cells could be separated from *SmoM2-Kmt2d*$^{Cf/Cf}$ because they had enhanced expression of the gene signatures specific to both *SmoM2* and *SmoM2-Kmt2d*$^{Cf/Cf}$ tumors.

In order to focus on differences in gene expression due to loss of *Kmt2d*, all further analysis was performed using the *SmoM2* and *SmoM2-Kmt2d*$^{Cf/Cf}$ tumor samples. As expected, principal component analysis and heatmaps with hierarchical clustering ($p <= 0.05$; *FC >= 1.5*) of bulk RNA-seq data from *SmoM2* and *SmoM2-Kmt2d*$^{Cf/Cf}$ tumor samples revealed two distinct clusters (Figures 4B and 4C; Table S3). Gene Ontology (GO) term analysis of the 1,004 genes downregulated in *SmoM2-Kmt2d*$^{Cf/Cf}$ tumors ($p <= 0.05$; *FC >= 1.5*) showed enrichment for genes associated with late stages of neuron differentiation, such as synapse organization, axonogenesis and regulation of membrane potential in the top 20 categories (Figure 4D). In contrast, GO term analysis of the 516 genes upregulated in *SmoM2-Kmt2d*$^{Cf/Cf}$ tumors ($p <= 0.05$; *FC >= 1.5*) showed enrichment for genes associated with cell processes involved in organ development including stem cell maintenance,

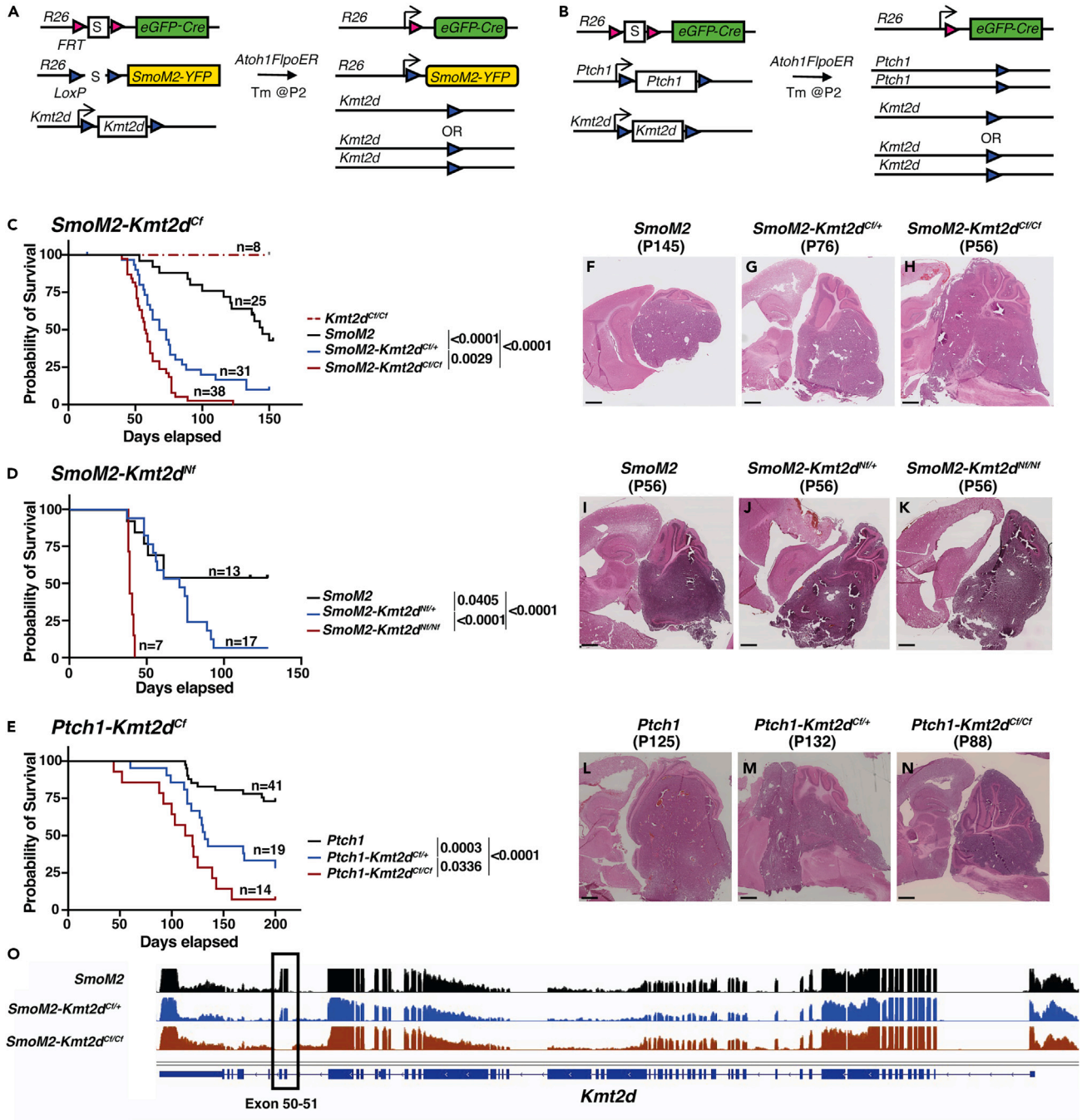

Figure 2. Two *Kmt2d* deletion mutations enhance tumor progression in SmoM2-driven SHH-MB and *Kmt2d* loss also enhances tumor progression when *Ptch1* is deleted

(A and B) Schematic showing the two sporadic mouse models of SHH-MB used, *SmoM2* (A) and *Ptch1*$^{fl/fl}$ (B) with and without a heterozygous or homozygous loss of *Kmt2d* (S: Stop of transcription/translation sequence).

(C–E) Kaplan-Meier curves (left) and statistics (right) for SHH-MB survival using a *SmoM2*-driven mouse model with a C-terminal (C) or N-terminus (D) heterozygous or homozygous mutation in *Kmt2d*, and a *Ptch1* loss-of-function model with C-terminal mutations of *Kmt2d*. Statistical significance was calculated using the log-rank test.

(F–N) Representative images of H&E-stained sagittal sections through the hemispheres from end stage *SmoM2*, *SmoM2-Kmt2d*$^{Cf/+}$, and *SmoM2-Kmt2d*$^{Cf/Cf}$ animals (F–H), *SmoM2*, *SmoM2-Kmt2d*$^{Nf/+}$, and *SmoM2-Kmt2d*$^{Nf/Nf}$ animals (I–K), and *Ptch1*, *Ptch1-Kmt2d*$^{Cf/+}$, and *Ptch1-Kmt2d*$^{Cf/Cf}$ animals (L–N). Scale bar: 1 mm.

(O) Overlay of RNA-seq data at the *Kmt2d* locus in *SmoM2* tumors (n = 5), *SmoM2-Kmt2d*$^{Cf/+}$ tumors (n = 2), and *SmoM2-Kmt2d*$^{Cf/Cf}$ tumors (n = 4). Also see Figure S2.

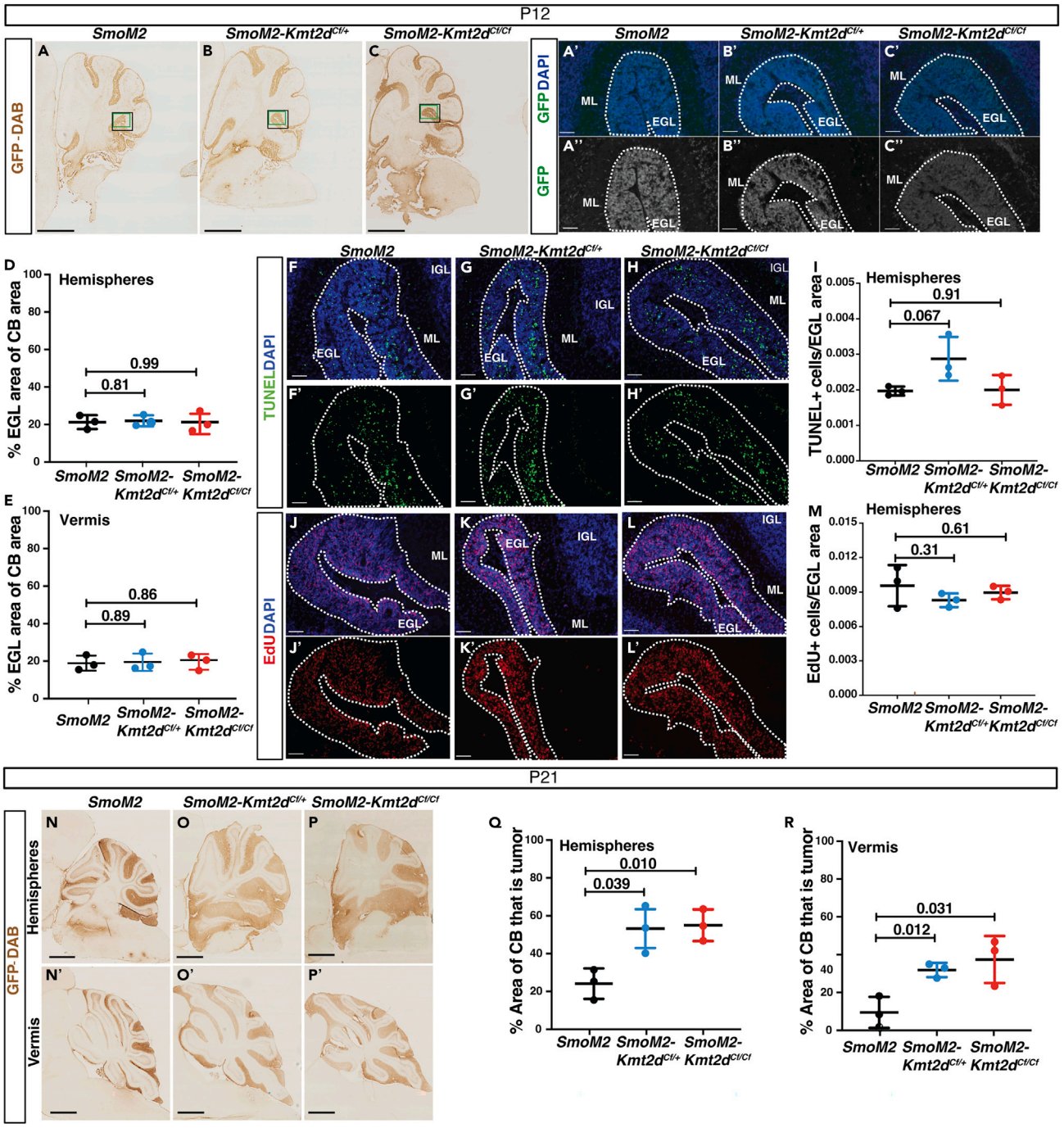

Figure 3. Heterozygous and homozygous mutations in *Kmt2d* promote tumor growth by P21

(A–C) Images of GFP stained (DAB) P12 sagittal sections from the hemispheres of *SmoM2*, *SmoM2-Kmt2d*$^{Cf/+}$, and *SmoM2-Kmt2d*$^{Cf/Cf}$ animals. Scale bar: 1 mm. Green boxes indicate where the images in (A′–C′) were taken and black boxes where the images in (F–L′) are from. (A′–C″) Images of overlayed Hoechst (blue) and GFP (green) staining (A′–C′) and GFP (white) staining (A″–C″). Scale bar: 100 μm.

(D and E) Quantification of the percentage of the cerebellum sectional area taken up by the EGL in the hemispheres (D) and vermis (E) of P12 *SmoM2*, *SmoM2-Kmt2d*$^{Cf/+}$, and *SmoM2-Kmt2d*$^{Cf/Cf}$ animals (n = 3 samples per genotype).

(F–H) Images of overlayed Hoechst (blue) and TUNEL (green) staining (or single channel TUNEL staining (F′– H′) in the EGL in the area indicated by the black box in (A–C). Scale bar: 250 μm.

(I) Quantification of the density of TUNEL+ cells in the EGL in the area of the hemispheres shown in (F–H) of *SmoM2*, *SmoM2-Kmt2d*$^{Cf/+}$, and *SmoM2-Kmt2d*$^{Cf/Cf}$ mice (n = 3 samples per genotype).

Figure 3. *Continued*

(J′–L′) Representative images of overlayed Hoechst (blue) and EdU (red) staining or single channel EdU (red) staining in the EGL in the area indicated by the black box in (A–C). Scale bar: 250 μm.

(M) Quantification of the density of EdU+ cells in the EGL in the area of the hemispheres shown (J–L) of *SmoM2*, *SmoM2-Kmt2d*$^{Cf/+}$, and *SmoM2-Kmt2d*$^{Cf/Cf}$ mice (n = 3 samples per genotype).

(N–P′) Images of GFP stained (DAB) P21 sagittal sections from the hemispheres (N–P) and vermis (N′–P′) of *SmoM2*, *SmoM2-Kmt2d*$^{Cf/+}$, and *SmoM2-Kmt2d*$^{Cf/Cf}$ animals. Scale bar: 1 mm.

(Q and R) Quantification of the percentage of the cerebellum sectional area taken up by the EGL/lesion in the hemispheres (Q) and vermis (R) of P21 *SmoM2*, *SmoM2-Kmt2d*$^{Cf/+}$, and *SmoM2-Kmt2d*$^{Cf/Cf}$ animals (n = 3 samples per genotype). All statistical significance was determined using an unpaired t-test comparing *Kmt2d* wildtype tumors to each of the *Kmt2d* mutants. Error bars: SD.

epithelial cell proliferation, and cell migration (including ameboidal-type cell migration, extracellular matrix organization, or EMT) (Figure 4E). Our results indicate that KMT2D normally promotes expression of genes involved in neural differentiation and indirectly inhibits genes that promote a progenitor state (possibly through activating inhibitors), thus KMT2D can be considered to function as a tumor suppressor.

Gene set enrichment analysis (GSEA) of genes upregulated in *SmoM2-Kmt2d*$^{Cf/Cf}$ tumors further highlighted that *SmoM2-Kmt2d*$^{Cf/Cf}$ tumors (indirectly) upregulate pathways associated with stem proliferation (Figure S3B), and genes/pathways that can regulate advanced stage cancers including TGFβ signaling, Notch signaling, and *MYC* (Figures S3C–S3E). Consistent with KMT2D normally being associated with activation of gene expression, *Smad7* and *Klf9*, suppressors of TGFβ and Notch signaling, respectively,[70–72] were significantly downregulated in *SmoM2-Kmt2d*$^{Cf/Cf}$ tumors (Table S3). Many of the key changes in gene expression identified by RNA-seq were validated by quantitative RT-PCR of RNA from GFP+ tumor cells isolated by FACS. RNA *in situ* and protein immunostaining of sections from additional tumor samples also provided validation and assessment of gene expression patterns. qRT-PCR analysis showed significant upregulation of *Atoh1*, *Sox2*, *Myc*, *Jag1*, *Hes1*, *Tgfbr2*, and *Smad3* and downregulation of *Neurod1* in *SmoM2-Kmt2d*$^{Cf/Cf}$ tumors (n = 6) compared to *SmoM2* (n = 5) (Figure 4F; Table S4). *Smad7* and *Klf9* appeared downregulated, although not to statistical significance ($p = 0.052$ and *0.126*, respectively). RNA *in situ* analysis of sagittal sections of primary tumors from *SmoM2* and *SmoM2-Kmt2d*$^{Cf/Cf}$ animals (n = 3 each) showed that *Kcnc3*, a gene associated with neural differentiation, was broadly expressed across *SmoM2* tumors whereas in *SmoM2-Kmt2d*$^{Cf/Cf}$ tumors expression was more patchy indicating less cells differentiate when *Kmt2d* is mutant (Figures S3F–S3I). *Myc* was expressed throughout the tumors of both genotypes and at higher levels in *SmoM2-Kmt2d*$^{Cf/Cf}$ tumors (Figures S3J–S3M). Double immuno-staining for NueroD1 protein, a neural differentiation gene significantly reduced based on qRT-PCR analysis, and Ki67 (proliferation marker), showed as expected that Ki67 and Neurod1 staining was largely complementary although some cells were double labeled (Figure S4). Consistent with the tumors having a classic histology, Ki67 was broadly expressed in both genotypes. However, in *SmoM2-Kmt2d*$^{Cf/Cf}$ tumors NeuroD1 high areas appeared reduced compared to in *SmoM2* tumors. Quantification of the fluorescence pixels in nuclei (Dapi+) demonstrated that Neurod1 had a lower density in *SmoM2-Kmt2d*$^{Cf/Cf}$ tumors compared to *SmoM2* tumors whereas Ki67 was not changed. Thus, KMT2D normally promotes a more differentiated state in SHH-MB tumor cells.

Network analysis for genes significantly upregulated in *SmoM2-Kmt2d*$^{Cf/Cf}$ tumors compared to *SmoM2* (Figure S5) revealed upregulation of genes that could enhance tumor growth, including genes previously shown to positively regulate cerebellar neural progenitor proliferation; *Sox2/9*,[56–60] *Atoh1*, and *Myc/Mycl*.[54,55] In addition, genes/pathways implicated in metastasis were upregulated in *SmoM2-Kmt2d*$^{Cf/Cf}$ tumors: TGFβ signaling (*Tgfbr2*, *Tgf1i1*, *Smad3*, and *Epha3*),[52,73,74] and Notch signaling (*Notch1*, *Hes1*, and *Jag1*),[50,53,75,76] the two pathways inhibited by *Smad7* and *Klf9* ($p \leq 0.05$; $FC \geq 1.5$).

In parallel to the RNA-seq data analysis, we performed ATAC-seq analysis of GFP+ cells from primary tumors, including a subset of the tumors in which RNA-seq was performed (Table S1). A comprehensive QC assessment of the ATAC-seq data showed a high signal-to-noise ratio (Figure S6A). Differential analysis based on peak annotations identified two distinct clusters of *SmoM2* and *SmoM2-Kmt2d*$^{Cf/Cf}$ primary tumors with a sub-cluster of tumors seen within the *SmoM2-Kmt2d*$^{Cf/Cf}$ cluster (Figure 5A). The differentially accessible chromatin regions displayed via a volcano plot further identified a separation of the *SmoM2* and *SmoM2-Kmt2d*$^{Cf/Cf}$ tumors and indicated two sub-clusters of *SmoM2-Kmt2d*$^{Cf/Cf}$ tumors (Figure 5B). A more detailed analysis of the ATAC-seq data showed that the global transcriptomic trends found using bulk RNA-seq between GFP+ *SmoM2* and *SmoM2-Kmt2d*$^{Cf/Cf}$ cells were retained in the global chromatin accessibility trends and the two corroborated with one another ($p <= 0.1$; $FC >= 1.5$), i.e., the genes with the most significant changes in mRNA and DNA peaks are in the concordant quadrants (red dots; Figure 5C). Similar to the gene expression trends seen in the RNA-seq analysis, ATAC-seq analysis identified an enhancement of open chromatin domains within neuronal differentiation genes (e.g., *NeuroD1)* in *SmoM2* tumors, whereas in *SmoM2-Kmt2d*$^{Cf/Cf}$ tumor cells open chromatin domains were enhanced in genes associated with TGFβ (*Smad3)* and Notch (*Hes1*) pathways (Figures 5D–5F; Table S5). In support of our hypothesis that loss of *Kmt2d* indirectly results in upregulation of the TGFβ and Notch pathways via decreased expression of inhibitors, ATAC-seq analysis showed diminution of open chromatin domains within *Klf9* and *Smad7* genes in *SmoM2-Kmt2d*$^{Cf/Cf}$ tumor cells, although not statistically significantly (Figures 5G and 5H; Table S5). Furthermore, motif enrichment analysis showed that motifs for pro-neural transcription factors (TFs) seen in differentiating neurons (e.g., NeuroD1 and ASCL1) were enriched in *SmoM2* tumors (Figure S6B; Table S5). In contrast, in *SmoM2-Kmt2d*$^{Cf/Cf}$ tumor cell DNA motifs bound by TFs associated with stem/progenitor cell populations (e.g., SOX2 and SOX9) were enriched (Figure S6B; Table S5), further validating our conclusions drawn from the RNA-seq data. *SmoM2-Kmt2d*$^{Cf/Cf}$ tumors also were enriched for motifs bound by SMAD3, a downstream effector of the TGFβ pathway (Figure S6B; Table S5). Interestingly, DNA motifs bound by ATOH1, a TF shown to augment SHH-MB tumor growth and metastasis when over-expressed in *Ptch1*$^{+/-}$ GCPs,[11] also were enriched in *SmoM2-Kmt2d*$^{Cf/Cf}$ tumors (Figure S6B; Table S5). Furthermore, motif enrichment analysis showed

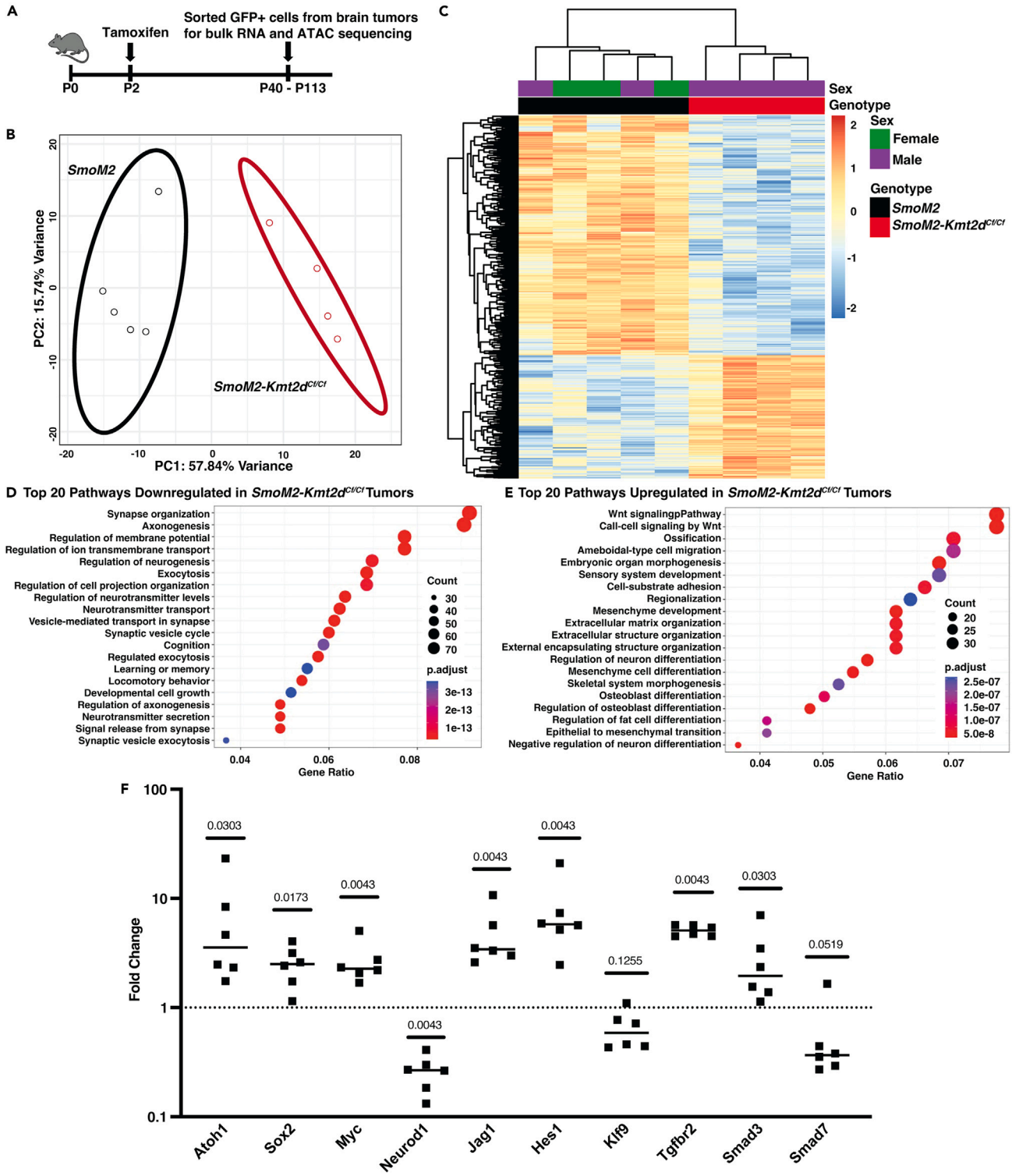

Figure 4. Bulk RNA-seq analysis reveals downregulation of neural differentiation genes and upregulation of Notch/TGFβ signaling and stem cell genes in *Kmt2d* mutant SHH-MB

(A) Experimental strategy to define the transcriptomic and chromatin accessibility landscape of tumors from *SmoM2*, *Smom2-Kmt2d*$^{Cf/+}$, and *SmoM2-Kmt2d*$^{Cf/Cf}$ mice.

(B) PCA analysis of RNA-seq data showing two distinct clusters of tumors from *SmoM2* (black oval) and *SmoM2-Kmt2d*$^{Cf/Cf}$ (red oval) animals.

Figure 4. *Continued*

(C) Heatmap analysis of RNA-seq data showing differentially expressed genes between *SmoM2* and *SmoM2-Kmt2d*$^{Cf/Cf}$ tumors (padj $\leq$ 0.05; FC $\geq$ 1.5).

(D and E) GO term analysis of the RNA-seq data showing the top downregulated (D) and upregulated (E) pathways in *SmoM2-Kmt2d*$^{Cf/Cf}$ tumors compared to *SmoM2* tumors.

(F) RT-qPCR analysis of indicated genes in GFP+ cells isolated by FACS from *SmoM2-Kmt2d*$^{Cf/Cf}$ tumors (n = 6) relative to *SmoM2* tumors (n = 5). Statistics were determined using the Mann-Whitney test. See also Tables S3 and S4, and Figures S3–S5.

enhancement of sequences bound by NEUROD1 and ASCL1 at the *NeuroD1* gene in *SmoM2* tumors and SMAD3 and MYC motifs in the *Smad3* gene in *SmoM2-Kmt2d*$^{Cf/Cf}$ tumors (Figures S6C and S6D; Table S5). Finally, network analysis of genes annotated at differentially accessible peaks enriched in *SmoM2-Kmt2d*$^{Cf/Cf}$ tumors showed Notch signaling forms a central node for several pathway and many of the other nodes are similar to the RNA-seq network analysis (Table S6; Figure S6E). Taken together, the bulk RNA-seq and ATAC-seq data demonstrate that loss of *Kmt2d* in SHH-MB primary tumors promotes a pro-tumorigenic transcriptional/epigenetic signature that includes genes and pathways associated with neural progenitor states and advanced disease, likely as a result of down regulation of suppressors of these genes/pathways and neural differentiation genes.

Loss of *Kmt2d* promotes local invasion in SHH-MB

Given that the RNA-seq and ATAC-seq data from SHH-MB tumors lacking *Kmt2d* indicate upregulation of pathways associated with aggressive tumors, we next asked whether the tumors have LMD and invade the surrounding brain regions, particularly the cerebellar white matter (WM) and brainstem (BS) at end stage or P150 in mice that survive and have primary tumors (Figure 6A–6D″; Table 1). Tumors of all genotypes had some LMD, but it was restricted to the hindbrain region. Strikingly, compared to *SmoM2* animals with 25% invasion into the WM (n = 4/16 mice) and 50% into the BS (8/16), significantly higher frequencies of local invasion were seen in *SmoM2-Kmt2d*$^{Cf/+}$ (WM: 12/15; BS:13/15) and *SmoM2-Kmt2d*$^{Cf/Cf}$ (WM: 18/18; BS: 18/18) (Table 1). The N-terminal mutation similarly increased local invasion from 57% in the WM (4/7) and BS (4/7) of *SmoM2* animals to 100% in the WM (8/8, p = 0.0192) and 87.5% into the BS (7/8, p = 0.0924) of *SmoM2-Kmt2d*$^{Nf/+}$ animals and 100% in the WM (6/6, p = 0.0337) and BS (6/6, p = 0.03337) of *SmoM2-Kmt2d*$^{Nf/Nf}$ animals (Table 1). Furthermore, in the *Ptch1* model of SHH-MB with a low amount of local invasion (WM: 4/10; BS: 3/10) a significantly higher percentage of *Ptch1-Kmt2d*$^{Cf/+}$ (WM: 9/10; BS: 8/10) and *Ptch1-Kmt2d*$^{Cf//Cf}$ (WM: 7/9; BS: 7/9) animals had WM and/or BS invasion at end stage or P200 (Figures S7A–S7B″; Table 1). These results provide *in vivo* evidence across two different mouse models of SHH-MB that a heterozygous or homozygous loss of *Kmt2d* promotes invasion of tumor cells locally.

Loss of *Kmt2d* promotes spinal cord metastasis in SHH-MB

We next asked whether loss of *Kmt2d* leads to increased metastatic disease in the spinal cord since it is prevalent in SHH-MB patients and since LMD was not seen anterior to the hindbrain in our models. A series of coronal sections of the entire spinal cord of each tumor bearing mouse was examined for cytology (H&E staining), and tumor cells were confirmed by expression of GFP and Ki67 (Figures 6E–6L″ and S6C–C″). Strikingly, we found that whereas only 33.3% of *SmoM2* (n = 12) animals had metastatic lesions along the spinal cord, *SmoM2-Kmt2d*$^{Cf/+}$ (n = 13) and *SmoM2-Kmt2d*$^{Cf/Cf}$ (n = 11) mice had a significant increase in tumors to 100% (Table 1). Furthermore, the percentage of the spinal cord containing metastatic tissue was significantly increased in *Kmt2d* mutants (Figure 6M). Clearing of a whole spinal cord from a *SmoM2-Kmt2d*$^{Cf/Cf}$ animal stained with antibodies to GFP (tumor cells) and Yoyo1 dye (nuclei) confirmed that metastatic tumors in *SmoM2-Kmt2d*$^{Cf/Cf}$ animals can form throughout the length of the spinal cord (Figures S7D–S7D‴). The N-terminal mutation of *Kmt2d* also significantly increased the percentage of mice with metastatic tumors (14.2% *SmoM2* vs. 62.5% *SmoM2-Kmt2d*$^{Nf/+}$ and vs. 100% *SmoM2-Kmt2d*$^{Nf/Nf}$) (Table 1) and the relative sizes of the metastatic lesions of homozygous mutants (Figure 6N). In the *Ptch1* model of SHH-MB the frequency of animals with metastatic disease was increased in the *Ptch1-Kmt2d*$^{Cf/Cf}$ animals compared to the *Ptch1* animals (33.3% *Ptch1* vs. 70% *Ptch1-Kmt2d*$^{Cf/+}$, p = 0.076 and vs. 100% *Ptch1-Kmt2d*$^{Cf/Cf}$, p = 0.0021) (Table 1). Similarly, the relative sizes of metastatic lesions were significantly increased in *Ptch1-Kmt2d*$^{Cf/Cf}$ (p = 0.019) but not *Ptch1-Kmt2d*$^{Cf/+}$ (p = 0.58) mutants (Figure 6O). In summary, we found that reduction of, or loss of *Kmt2d* in two mouse models of SHH-MB greatly promotes metastatic disease to the spinal cord.

Metastatic and primary tumors have similar transcriptomic and chromatin accessibility profiles

Given that the deletion of *Kmt2d* in mouse models of SHH-MB results in invasive and metastatic disease, we compared the transcriptomes of primary and metastatic GFP+ tumor cells from the same *SmoM2-Kmt2d*$^{Cf/Cf}$ animals (Tables S1 and S7). Surprisingly, there were only 41 differentially expressed genes between the primary and metastatic tumors (Figure 7A; Table S7) (*p <= 0.05; FC >= 1.5*). Furthermore, 19 of the 41 differentially expressed genes might have been from contaminating infiltrating immune cells or spinal cord neurons/glia based on the genes over-expressed, low read counts and/or high variability between samples (bold font genes in Table S7). Interestingly, among the remaining genes, a subset of the 16 genes over-expressed in metastatic cells has been shown to be associated with poor prognosis in cancer (*Sparc*, *Nr4a1*, *Itgb5*, *Fos*, and *Fosb*).[77–81]

A similarity and stability of the transcriptional landscapes of the primary and metastatic compartments of *SmoM2-Kmt2d*$^{Cf/Cf}$ animals was also seen when comparing RNA-seq data to *SmoM2* primary tumors using PCA analysis (Figure S8A) and hierarchical clustering (Figure 7B; Table S8), as the *SmoM2-Kmt2d*$^{Cf/Cf}$ primary and metastatic tumors clustered together and were separated from the *SmoM2* primary tumors. Pathway analysis similarly confirmed that *SmoM2-Kmt2d*$^{Cf/Cf}$ tumor cells from the primary and metastatic compartments both had

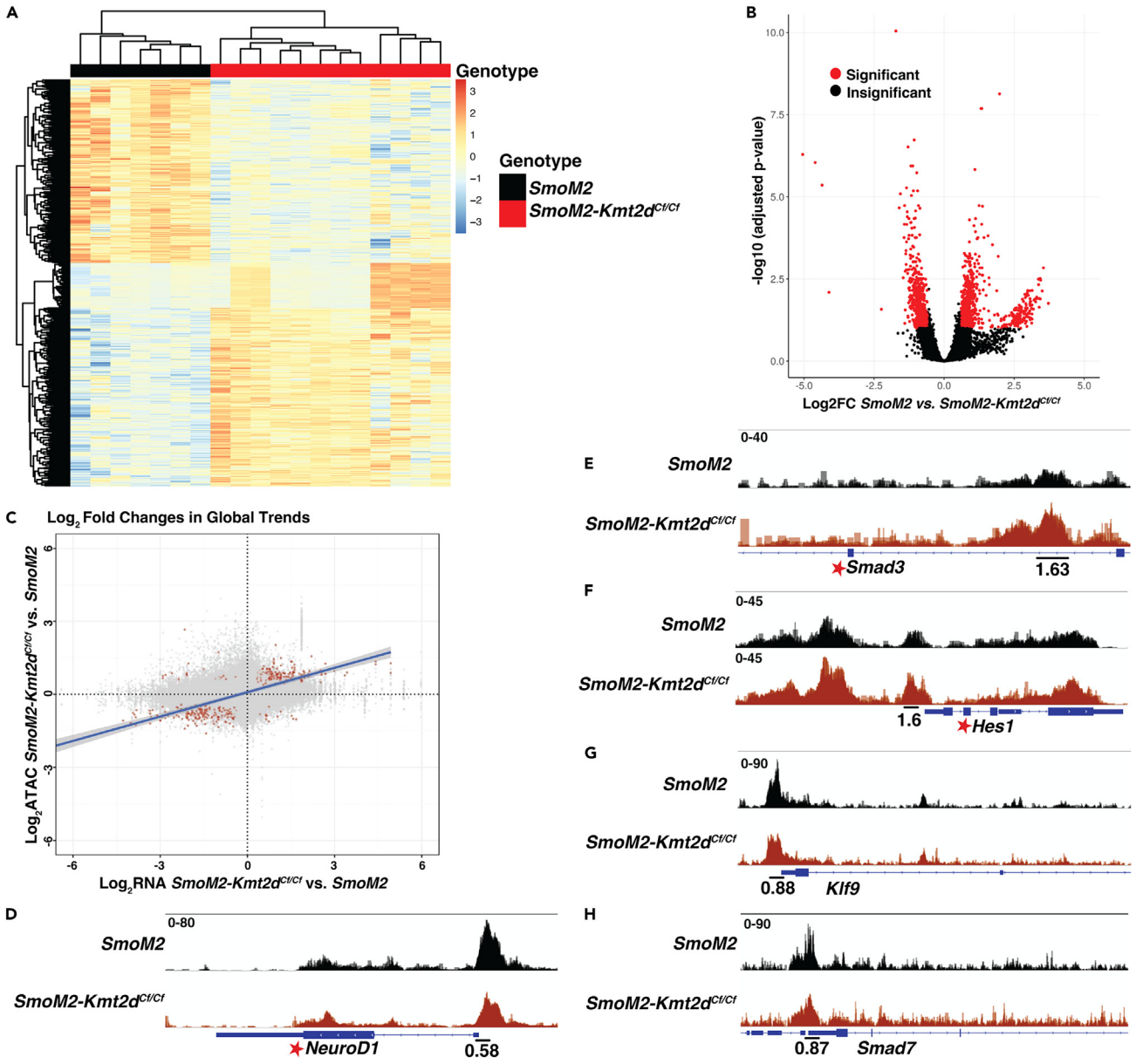

Figure 5. ATAC-seq data analysis reveals differences in DNA accessibility of pathways associated with neural differentiation and advanced cancer in *SmoM2-Kmt2d*$^{Cf/Cf}$ vs. *SmoM2* tumor

(A) Heatmap showing the clustering of differential peaks between *SmoM2* and *SmoM2-Kmt2d*$^{Cf/Cf}$ tumors (FC ≥ 1.5, padj ≤ 0.1).

(B) Volcano plots displaying the differentially accessible chromatin regions in *SmoM2-Kmt2d*$^{Cf/Cf}$ compared to *SmoM2* tumor cells (FC ≥ 1.5, padj ≤ 0.1).

(C) Comparison of the log2 fold changes (red indicates FC ≥ 1.5, padj ≤ 0.1) in global trends in *SmoM2-Kmt2d*$^{Cf/Cf}$ tumor cells compared to *SmoM2* in the RNA-seq and ATAC-seq datasets.

(D–H) ATAC-seq plots showing regions of increased and decreased chromatin accessibility at specific gene loci in *SmoM2-Kmt2d*$^{Cf/Cf}$ (n = 12) compared to *SmoM2* (n = 7) primary tumors. The number below indicates the FC in a single 500-bp peak. Fold changes with a padj ≤ 0.1 are indicated with a star. Also see Figure S6 and Tables S5 and S6.

downregulation of genes associated with neuronal differentiation and upregulation of genes associated with organ morphogenesis and EMT compared to primary *SmoM2* tumor cells (Figures S8B and S8C). Furthermore, network enrichment analysis comparing *SmoM2* mutant primary tumors to *SmoM2-Kmt2d*$^{Cf/Cf}$ primary and metastatic tumors showed upregulation of previously identified genes and pathways that can drive progenitor states and tumor progression: *Sox2/9*, *Myc*, *Atoh1*, and TGFβ and Notch pathway genes (Figure 7C). Given that some of the upregulated genes identified by the RNA-seq data analysis are not specific to the SHH-MB subgroup, we compared the *SmoM2-Kmt2d*$^{Cf/Cf}$

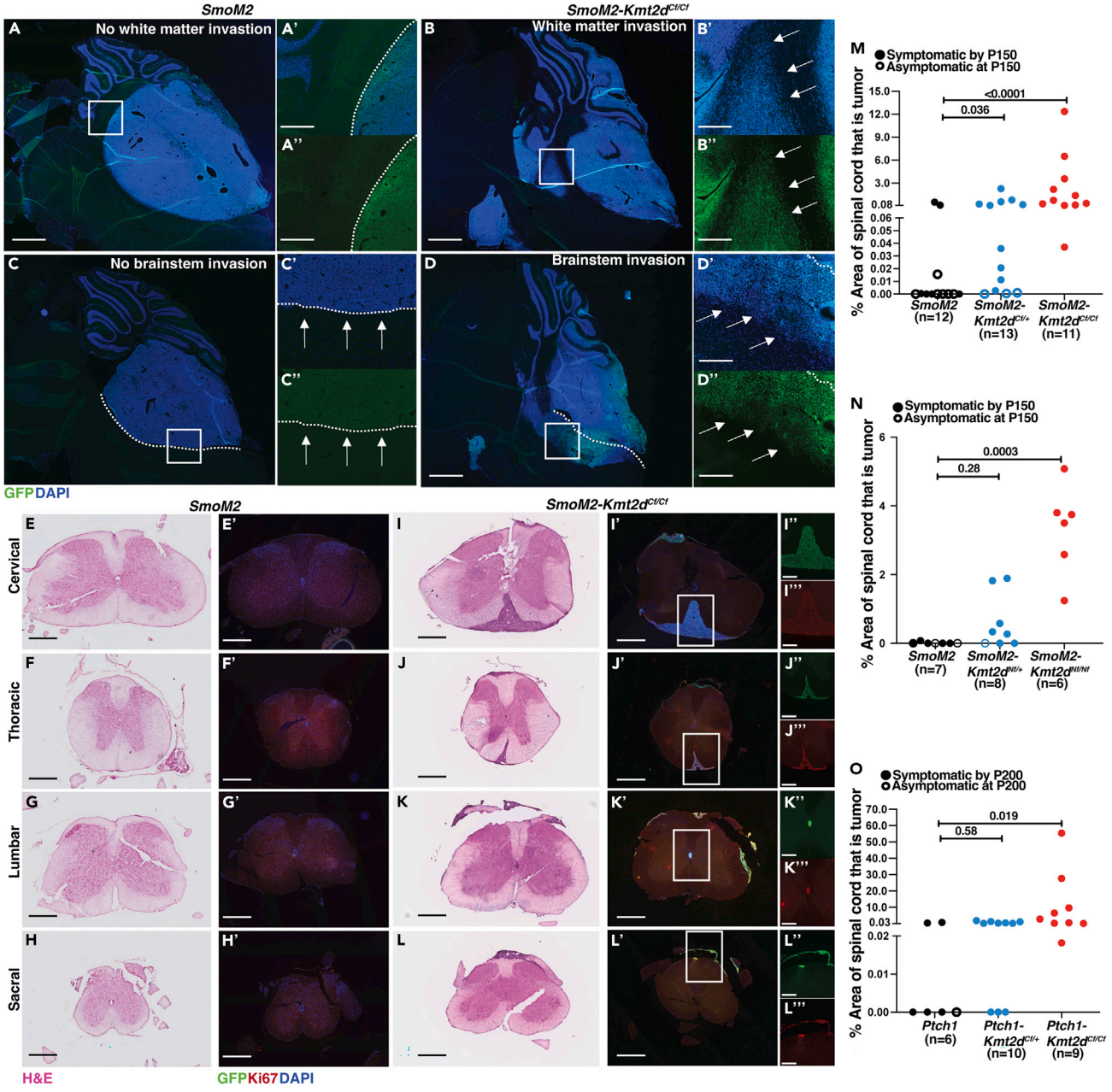

Figure 6. Loss of *Kmt2d* in two models of SHH-MB promotes local cell invasion and spinal cord metastasis

(A–D″) Representative images of sagittal sections from end stage tumors stained with Hoechst (blue) and GFP (green) without tumor cell invasion into the white matter (WM) (A, A′, A″) or with tumor cell invasion into the WM (B, B′, B″), and without tumor cell invasion into the brainstem (BS) (C, C′, C″) or with tumor cell invasion into the BS (D, D′, D″). Overlayed Hoechst and GFP images of the whole cerebellum are shown in (A–D) (Scale bar: 1 mm). Overlayed Hoechst and GFP images in the specific regions indicated by rectangles in (A) are shown in (A′–D′) and single channel GFP-staining of the same regions in (A″–D″) (Scale bar: 250 μm).

(E–H) Representative sections at the rostral-caudal levels indicated of spinal cords stained with H&E from *SmoM2* animals without metastasis (Scale bar: 500 μm).

(E′–H′) Adjacent sections stained with Hoechst, GFP (green) and Ki67 (red) (Scale bar: 500 μm).

(I–L) Representative sections of spinal cords stained with H&E from *SmoM2-Kmt2d*$^{Cf/Cf}$ animals (Scale bar: 500 μm).

(I′–L′) Fluorescence images of adjacent sections stained with Hoechst, GFP (green) and Ki67 (red) (Scale bar: 500 μm). Single channel GFP (I″-L″) and Ki67 (I‴–L‴) staining of metastatic tumors in the spinal cord (Scale bar: 250 μm).

Figure 6. *Continued*

(M–O) Quantification of the percentage of sectional spinal cord area taken up by tumor in >30 sections per mouse in the *SmoM2*-driven model of SHH-MB with and without a *Kmt2d* C-terminal mutation (M) or *Kmt2d* N-terminal mutation (N), and in the *Ptch1* model (O). Open dots indicate animals that did not show symptoms of tumor burden at P150 (*SmoM2* models) or P200 (*Ptch1* model) but had primary tumors. All statistical significance was determined using an unpaired t-test comparing *Kmt2d* wildtype tumors to each of the *Kmt2d* mutants. Also see Figure S7.

primary and metastatic tumor cell expression profiles to genes associated with the 4 subgroups of MB (Figure S8D). Although some primary and metastatic *SmoM2-Kmt2d*$^{Cf/Cf}$ tumor samples express genes associated with subgroups of MB other than SHH, there was enrichment for an SHH-MB signal in the tumors (Figure S8D).

A QC assessment of the ATAC-seq data from *SmoM2-Kmt2d*$^{Cf/Cf}$ metastatic tumors showed a high signal-to-noise ratio (Figure S6A). ATAC-seq analysis of *SmoM2-Kmt2d*$^{Cf/Cf}$ metastatic tumors in addition to *SmoM2* and *SmoM2-Kmt2d*$^{Cf/Cf}$ primary tumors showed the predicted decrease in chromatin accessibility in neural differentiation associated genes (e.g., *Kcnc3*) and in *Klf9* and *Smad7* in metastatic as well as primary *SmoM2-Kmt2d*$^{Cf/Cf}$ tumors and an increase in accessibility of tumor genes associated with the Notch pathway (*Jag1*), TGFβ pathway (*Smad3*), and progenitor cell populations (*Sox2*) compared to *SmoM2* (Figures S8E–S8J; Tables S5 and S9). Thus, our transcriptomic and epigenetic data reveal that loss of *Kmt2d* in *SmoM2* tumors promotes MB tumor progression and metastasis through the (indirect) upregulation of the TGFβ and Notch oncogenic pathway genes, as well as *Myc*, *Sox2/9*, and *Atoh1*, all of which have been previously implicated as key drivers of tumor growth and metastasis in MB.

DISCUSSION

Our study demonstrates that in the context of mouse models of SHH-MB, *Kmt2d* is a tumor suppressor that inhibits tumor growth, invasion into the hindbrain and metastatic spread to the spinal cord, in part through promoting neural differentiation. Furthermore, heterozygous loss-of-function mutations in *Kmt2d*, as seen in patients, are sufficient to drive SHH-MB to advanced stages of the disease via haploinsufficiency. Metastasis is a hallmark of late-stage disease and responsible for the highest number of cancer-related fatalities. However, the molecular drivers of metastatic disease, especially in brain cancers, remain largely unknown in part due to a lack of robust animal model systems. One approach used to identify candidate genes that drive SHH-MB dissemination into the leptomeninges and spinal cord metastasis was an insertional mutagenesis screen that mobilizes a Sleeping Beauty transposon[81] in cerebellar GCPs of *Ptch*$^{+/-}$ animals.[20] Follow up studies showed that over-expression of *Eras*, *Lhx1*, *Ccrk*, *Arnt*, *Gdi2* or activated AKT are sufficient to increase dissemination and metastasis when combined with forced expression of *Shh* by viral infection of GCPs and transplantation.[20,82,83] Another study identified circulating tumor cells in the blood using this and other mouse transplantation models and analysis of human tumor cells. The CCL2-CCR2 axis was identified as upregulated in disseminated cells and shown to be sufficient to enhance metastasis of GCPs expressing SHH.[8] In a separate model, over-expression of *Atoh1* in GCPs of *Ptch1*$^{+/-}$ mice using a conditional transgene approach demonstrated ATOH1 can promote tumor penetrance and spinal cord metastasis to 100%.[11] While these papers identified genes that when over-expressed in mouse models can facilitate metastasis of GCPs with constitutive SHH signaling, their relevance to the normal genetic changes seen in SHH-MB are not clear.

Loss of *Kmt2d* in SHH-MB leads to downregulation of neural differentiation and upregulation of genes/pathways associated with a progenitor state

Bulk RNA-seq analysis and concordant ATAC-seq results revealed that *SmoM2-Kmt2d*$^{Cf/Cf}$ primary tumors are distinct from *SmoM2* tumors, and that *SmoM2-Kmt2d*$^{Cf/+}$ tumors share upregulated genes with both tumor genotypes. Whether *SmoM2-Kmt2d*$^{Cf/+}$ tumors upregulate the genes seen in *Kmt2d* homozygous mutant tumors and maintain the genes expressed in *Kmt2d* WT tumors or instead have a mixture of both cell phenotypes is not clear from our bulk RNA-seq data. Given the function of KMT2D in augmenting gene expression, loss of *Kmt2d* is predicted to downregulate genes. Of likely relevance, the differentially expressed genes significantly downregulated based on RNA-seq analysis in *SmoM2-Kmt2d*$^{Cf/Cf}$ primary tumors are greatly enriched for genes/pathways involved in neural differentiation, and two genes were validated with qRT-PCR and/or analysis of protein/RNA in sections. *Kcnc3* RNA or NeuroD1 protein were detected broadly across *SmoM2* tumors, as was Ki67, whereas in *SmoM2-Kmt2d*$^{Cf/Cf}$ tumors the *Kcnc3*/NeuroD1 domains were diminished. These results indicate KMT2D promotes expression of neural differentiation genes, even in progenitors within the tumors and therefore that KMT2D promotes the transition of GCPs from a progenitor to differentiated state. Loss of *Kmt2d* therefore promotes a progenitor state. Consistent with this, in E18.5 embryos lacking *Kmt2d* in GCPs, the proportion of differentiated cells in the EGL (inner EGL) is reduced. Furthermore, in tumors with a partial or complete loss of *Kmt2d*, genes that regulate a GCP progenitor state are upregulated. In addition, some of these genes have been associated with advanced cancer in SHH-MB, including *Sox2*[56–60] and *Atoh1*.[11] However, none of the genes identified by Sleeping Beauty enabled mutagenesis[20,82,83] were found to be differentially expressed in *SmoM2-Kmt2d*$^{Cf/Cf}$ tumors compared to *SmoM2* although some genes (*Akt2*, *Gdi2*, *Arnt*, and *Lhx1*) were expressed at high levels in both genotypes (Table S10).

In *SmoM2-Kmt2d*$^{Cf/Cf}$ tumors lacking *Kmt2d*, genes in the TGFβ[52,73,74] and Notch pathway[50,53,75,76] which can increase oncogenesis are significantly upregulated in the RNA-seq data compared to *SmoM2* primary tumors. Interestingly, suppressors of TGFβ and Notch signaling, *Smad7*[70] and *Klf9*,[71,72] respectively, are significantly downregulated in *SmoM2-Kmt2d*$^{Cf/Cf}$ tumor cell RNA-seq data. While *Smad7* was close to significantly decreased based on qRT-PCR ($p = 0.052$) in *SmoM2-Kmt2d*$^{Cf/Cf}$ tumors compared to *SmoM2*, the reduction in *Klf9* ($p = 0.126$) was not. Nevertheless, a significant reduction of *Klf9* in a specific progenitor pool might lower Notch signaling. Thus, *Smad7* and *Klf9* expression

Table 1. Summary of the phenotypes of mice with a heterozygous or homozygous *Kmt2d*^{Cf} or *Kmt2d*^{Nf} mutations in two models of SHH-MB

Genotype	% White Matter invasion	% Brainstem invasion	% Spinal cord Metastasis
SmoM2	25 (n = 16)	50 (n = 16)	33.3 (n = 12)
SmoM2-Kmt2d$^{Cf/+}$	80 (n = 15) [0.0011]	86.6 (n = 15) [0.0145]	100 (n = 13) [0.0002]
SmoM2-Kmt2d$^{Cf/Cf}$	100 (n = 18) [<0.0001]	100 (n = 18) [0.0003]	100 (n = 11) [0.0004]
SmoM2	57.1 (n = 7)	57.1 (n = 7)	14.2 (n = 7)
SmoM2-Kmt2d$^{Nf/+}$	100 (n = 8) [0.0192]	87.5 (n = 8) [0.0924]	62.5 (n = 8) [0.0286]
SmoM2-Kmt2d$^{Nf/Nf}$	100 (n = 6) [0.0337]	100 (n = 6) [0.0337]	100 (n = 6) [0.0010]
Ptch1	40 (n = 10)	30 (n = 10)	33.3 (n = 6)
Ptch1-Kmt2d$^{Cf/+}$	90 (n = 10) [0.0095]	80 (n = 10) [0.0123]	70 (n = 10) [0.0762]
Ptch1-Kmt2d$^{Cf/Cf}$	77.7 (n = 9) [0.0479]	77.7 (n = 9) [0.0186]	100 (n = 9) [0.0021]

% White Matter invasion: the percentage of animals with a primary tumor (number give in brackets) that had tumor cell invasion in the white matter.
% Brainstem invasion: the percentage of animals with a primary tumor (number give in brackets) that had tumor cell invasion into the brainstem.
% Tumor metastasis: the percentage of animals with a primary tumor (number give in brackets) that had metastasis to the spinal cord.
All animals either were sacrificed when they showed signs or at P150 (*SmoM2* models) or P200 (*Ptch1* model) and only mice with primary tumors when analyzed.
Statistical significance [p value] for each parameter was calculated using Chi-square test for comparing proportions between *Kmt2d*$^{fl/+}$ or *Kmt2d*$^{fl/fl}$ mutant tumors and *Kmt2d*$^{+/+}$ tumors of the same model.

might normally be enhanced by KMT2D in a particular cell type and a decrease in mutant tumor cells could contribute to the increase in expression of Notch and TGFβ pathway genes.

Key candidate up- and downregulated genes were confirmed by qRT-PCR analysis of GFP+ cells isolated from *SmoM2* and *SmoM2-Kmt2d*$^{Cf/Cf}$ tumors. Furthermore, ATAC-seq data from *SmoM2* and *SmoM2-Kmt2d*$^{Cf/Cf}$ primary tumors revealed trends in motif enrichment and open chromatin in concordance with the RNA-seq data. While the trends observed in the ATAC-seq data are subtle, we hypothesize that the overall effects are bolstered by the concomitant changes across a number of genes within the same pathway and across different pathways (Tables S5, S6, and S9). Furthermore, the analysis of RNA/protein expression on tumor sections of differentiation and proliferation markers showed that the tumors are heterogeneous, with *SmoM2-Kmt2d*$^{Cf/Cf}$ tumors having a reduction in the areas expressing high Neurod1 and *Kcnc3* compared to SmoM2. We predict that heterozygous mutations in *KMT2D* shift the transcriptional and epigenetic landscape of human SHH-MBs to a more aggressive tumor gene signature that enhances metastasis through promoting a progenitor state and enhancing Notch/TGFβ signaling, likely in a subset of cells that go on to form the bulk of the tumor.

Primary and metastatic tumors share a transcriptional gene signature

Differential transcriptomic and epigenomic analysis of *SmoM2* primary tumors and *SmoM2-Kmt2d*$^{Cf/Cf}$ primary and metastatic spinal cord tumors showed little segregation between the *SmoM2-Kmt2d*$^{Cf/Cf}$ primary and metastatic tumors using supervised on unsupervised clustering techniques. Moreover, the metastatic and primary *SmoM2-Kmt2d*$^{Cf/Cf}$ tumor cells (GFP+) from the same mice had very similar transcriptional landscapes, with only ~20 genes being clearly differentially expressed (Tables S7 and S8). Some genes involved in handling hypoxia[84–86] were expressed in both primary and metastatic tumors (Tables S8 and S10). This result is consistent with SHH-MB primary tumors in our mouse models growing on the surface of the brain and thus being in a hypoxic environment as in spinal cord metastases. Unlike our finding of largely similar transcriptional profiles in primary and metastatic *SmoM2-Kmt2d*$^{Cf/Cf}$ tumor cells, when *Atoh1* alone was over-expressed in a *Ptch1* model of SHH-MB, bulk RNA-seq comparing primary and metastatic tumors identified extensive differential gene expression.[11,20] Additional mutational and epigenetic analysis and clinical outcomes data of limited human MB samples support a similar conclusion.[11,20] Nevertheless, studies have shown matched MB primary and metastatic tumors maintain their subgroup-specific global transcriptional profiles.[87] One possible explanation for our finding is that mutations in genes like *KMT2D* that encode epigenetic modifiers can result in global transcriptional changes that are sufficient to drive metastasis as well as enhanced tumor growth in most primary tumor cells. Finally, of note, although *SmoM2-Kmt2d*$^{Cf/Cf}$ primary and metastatic tumors preferentially express genes associated with SHH-MB (Figure S8D), they have upregulation of Notch pathway genes and *MYC*, as well as upregulation of *Bcl2* (Table S3) which are associated with group 3 MB and have been implicated in mouse models of Group 3 MB that express MYC.[50,53,88,89] Thus, mutations in chromatin remodeling genes might partially blur the lines between the transcriptional profiles of MB subgroups.

Heterozygous mutations in *Kmt2d* are sufficient to cause metastatic disease

Whereas we did not find that two distinct homozygous *Kmt2d* mutations in all cerebellar lineages drive tumorigenesis, we did find that in two mouse models of SHH-MB (*SmoM2* expression or *Ptch1* homozygous loss) these same mutations in the heterozygous state are sufficient to dramatically accelerate tumor growth, and augment local invasion into the hindbrain and metastasis to the spinal cord. While there might be subtle differences in the extent of promotion of tumor growth rate, local invasion and spinal cord metastasis between the two mutations (Table 1), both mutations significantly increase the percentage of mice that develop primary tumors and metastatic disease when SmoM2 is

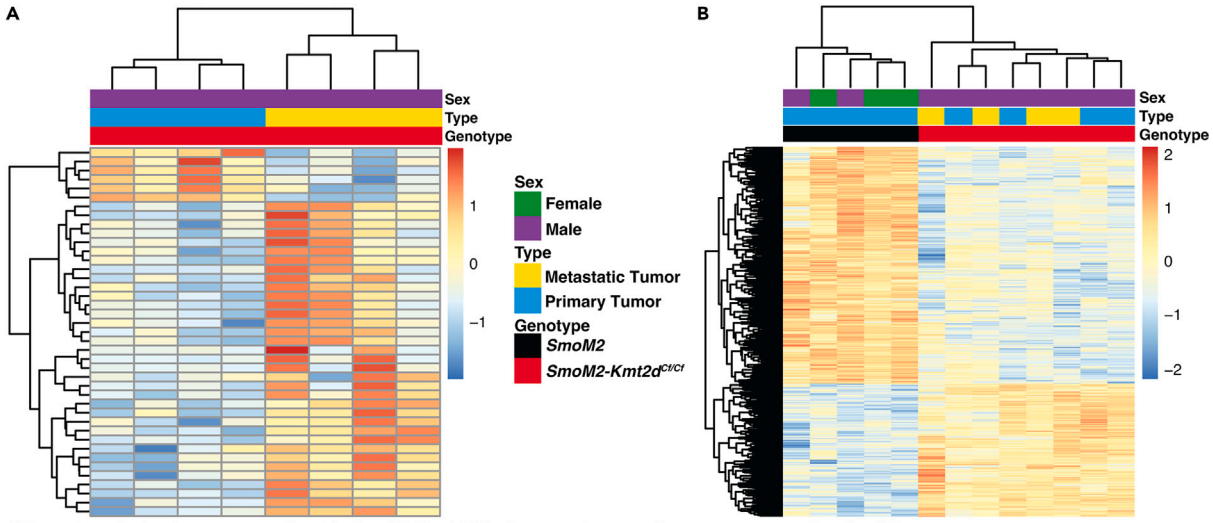

C Network analysis of genes upregulated in *SmoM2-Kmt2d*$^{ct/ct}$ primary and metastatic tumors compared to *SmoM2* tumors

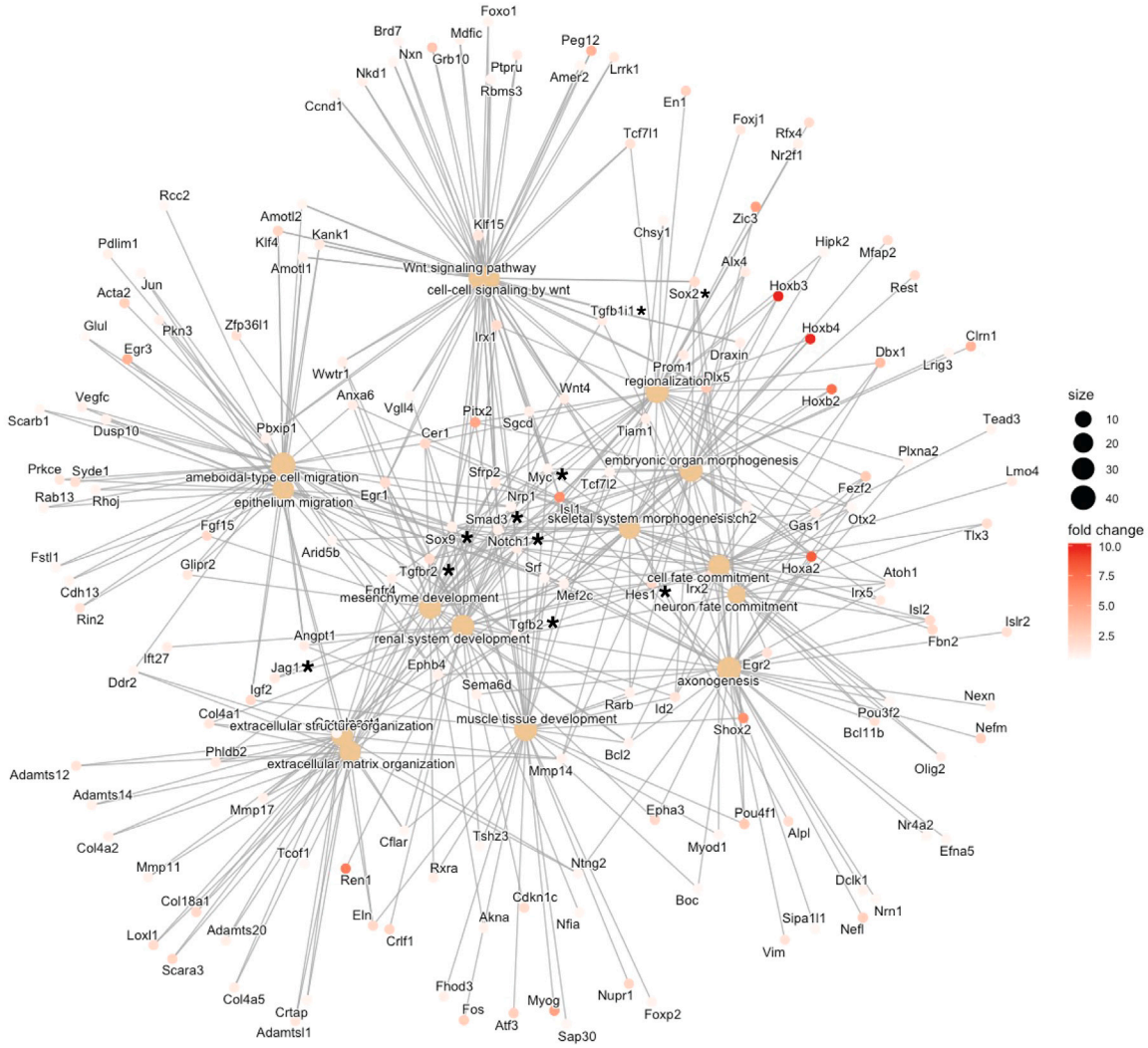

Figure 7. Transcriptional profiling of *SMoM2-Kmt2d*$^{Cf/Cf}$ primary and metastatic tumors compared to *SmoM2* reveals upregulation of genes/pathways associated with aggressive cancer

(A) Heatmap analysis of bulk RNA-seq showing differentially expressed genes between *SmoM2-Kmt2d*$^{Cf/Cf}$ primary and metastatic tumors. (*p <= 0.05; FC >= 1.5*). See also Table S7.

(B) Heatmap analysis of bulk RNA-seq showing differentially expressed genes between *SmoM2* primary tumors and *SmoM2-Kmt2d*$^{Cf/Cf}$ primary and metastatic tumors. (*p <= 0.05; FC >= 1.5*). See also Table S8.

(C) Network enrichment analysis of genes upregulated in *SmoM2-Kmt2d*$^{Cf/Cf}$ primary and metastatic tumors compared to *SmoM2* primary tumors. Also see Figure S8.

expressed in GCPs. Comparison of the effect of one mutation (C-terminal) in our sporadic *SmoM2* and *Ptch1* models further showed that heterozygous (or homozygous) loss of *Kmt2d* greatly increases incidence of primary tumors and spinal cord metastasis, even when disease progression and incidence are different in the two models. We predict that *KMT2D* mutations will drive aggressive disease in the context of all the SHH pathway activating mutations seen in human SHH-MB. The clinical relevance of the mouse models developed in this study is highlighted by two aspects of patient tumor biology that are recapitulated in these models: (a) mono-allelic loss-of-function mutations in *KMT2D* are associated with SHH-MB tumorigenesis[34,43,45,46] and (b) metastatic disease in SHH-MB patients occurs most frequently intracranially or along the spine.[8] Of note, while the tumors of all genotypes had LMD around the hindbrain/cerebellum, the dissemination did not spread to more anterior brain regions, unlike other models of SHH-MB metastasis.[8,11,83,90] This result could indicate that the kind metastasis-promoting gene undergoing a secondary mutation will influence the site of LMD, brain invasion and metastasis. Our findings thus highlight the importance of testing the involvement of genes in addition to *KMT2D* that are preferentially mutated in the β-subtype of SHH-MB, as well as other subtypes, to identify likely prognostic markers for patients at high risk of recurrent metastasis.

Limitations of the study

One limitation of the study is that for practical reasons the transcriptomic and epigenomic analyses were performed in only one of the 3 mouse models of SHH-MB, although we expect similar results with the N-terminal *Kmt2d* deletion mutation and in the *Ptch1* model. In addition, the sample sizes for the *SmoM2-Kmt2d*^{Nf} and *Ptch1-Kmt2d*^{Cf} SHH-MB models might not be large enough to detect slight differences in tumor biology caused by the N- and C-terminal deletions of *Kmt2d* or by aberrantly activating SHH signaling through expression of SmoM2 versus loss of *Ptch1*. Beyond the scope of the study, functional studies to test the impact of removing the candidate genes identified by the transcriptomic/epigenomic analyses will be important. An additional possible long-term study would be to validate candidate direct and indirect targets of KMT2D, as this could contribute to both our understanding of the genetics of SHH-MB tumor metastasis and the molecular functions of KMT2D.

STAR★METHODS

Detailed methods are provided in the online version of this paper and include the following:

- KEY RESOURCES TABLE
- RESOURCE AVAILABILITY
  - Lead contact
  - Materials availability
  - Data and code availability
- EXPERIMENTAL MODEL AND STUDY PARTICIPANT DETAILS
  - Animal work and breeding
- METHOD DETAILS
  - Tissue processing
  - Microscopy
  - Histology, Immunofluorescence and Immunohistochemistry
  - TUNEL staining
  - EdU (5-ethynyl-2′-deoxyuridine) Injection and staining
  - Clearing and light sheet imaging
  - RNA *in situ* hybridization
  - qRT-PCR analysis of GFP+ tumor cell RNA
  - Western Blot
  - Sample preparation for sequencing experiments
  - RNA-seq sample preparation
  - ATAC-seq sample preparation
- QUANTIFICATION AND STATISTICAL ANALYSIS
  - E18.5 GCP proliferation rate, P12/21 TUNEL, KI67, NeuroD1 and EdU quantification
  - Quantification of CB and Tumor area
  - Transcriptome analysis

- Epigenome analysis
- Statistical analysis

SUPPLEMENTAL INFORMATION

Supplemental information can be found online at https://doi.org/10.1016/j.isci.2023.107831.

ACKNOWLEDGMENTS

We are grateful to members of the Joyner lab for helpful comments throughout the work, in particular to I-Li Tan during the early stages of the work. We thank the Memorial Sloan Kettering Cancer Center Flow Cytometry Core, Integrated Genomics Operations Core Facility and the Center for Comparative Medicine and Pathology for technical support, and James Muller for assistance with 3D imaging. We also thank Daniel Medina-Cano from the Thomas Vierbuchen lab and Yanhong Yang from the Viviane Tabar lab at MSKCC for reagents. We are grateful to Lucia Grandison and Derek Lao for technical assistance and to Cara Monaco for helping prepare the manuscript. Some of the schematics in the graphical abstract were created using Biorender.com. The research was supported by grants to A.L.J. from the NCI (R01CA192176) and MSK Functional Genomics Initiative (GC24221), to S.E. from a Francois Wallace Monahan Fellowship and a National Cancer Institute Cancer Center Support Grant [P30 CA008748-48].

AUTHOR CONTRIBUTIONS

Conceptualization: R.M.S. and A.L.J.; Methodology: R.M.S. and A.L.J.; Investigation: R.M.S., H.M., D.N.S., S.E., Z.L., and N.S.B.; Formal Analysis: R.M.S., R.K., H.M., S.E., and A.L.J.; Resources: K.G.; Manuscript Preparation: R.M.S. and A.L.J.

DECLARATION OF INTERESTS

The authors declare no competing interests.

INCLUSION AND DIVERSITY

We support inclusive, diverse and equitable conduct of research.

Received: August 24, 2022
Revised: March 29, 2023
Accepted: September 1, 2023
Published: September 9, 2023

REFERENCES

1. Taylor, M.D., Northcott, P.A., Korshunov, A., Remke, M., Cho, Y.J., Clifford, S.C., Eberhart, C.G., Parsons, D.W., Rutkowski, S., Gajjar, A., et al. (2012). Molecular subgroups of medulloblastoma: the current consensus. Acta Neuropathol. *123*, 465–472. https://doi.org/10.1007/s00401-011-0922-z.
2. Rossi, A., Caracciolo, V., Russo, G., Reiss, K., and Giordano, A. (2008). Medulloblastoma: from molecular pathology to therapy. Clin. Cancer Res. *14*, 971–976. https://doi.org/10.1158/1078-0432.CCR-07-2072.
3. Northcott, P.A., Dubuc, A.M., Pfister, S., and Taylor, M.D. (2012). Molecular subgroups of medulloblastoma. Expert Rev. Neurother. *12*, 871–884. https://doi.org/10.1586/ern.12.66.
4. Northcott, P.A., Jones, D.T.W., Kool, M., Robinson, G.W., Gilbertson, R.J., Cho, Y.J., Pomeroy, S.L., Korshunov, A., Lichter, P., Taylor, M.D., and Pfister, S.M. (2012). Medulloblastomics: the end of the beginning. Nat. Rev. Cancer *12*, 818–834. https://doi.org/10.1038/nrc3410.
5. Gilbertson, R.J., and Ellison, D.W. (2008). The origins of medulloblastoma subtypes. Annu. Rev. Pathol. *3*, 341–365. https://doi.org/10.1146/annurev.pathmechdis.3.121806.151518.
6. Meirson, T., Gil-Henn, H., and Samson, A.O. (2020). Invasion and metastasis: the elusive hallmark of cancer. Oncogene *39*, 2024–2026. https://doi.org/10.1038/s41388-019-1110-1.
7. Kciuk, M., Gielecińska, A., Budzinska, A., Mojzych, M., and Kontek, R. (2022). Metastasis and MAPK Pathways. Int. J. Mol. Sci. *23*, 3847. https://doi.org/10.3390/ijms23073847.
8. Garzia, L., Kijima, N., Morrissy, A.S., De Antonellis, P., Guerreiro-Stucklin, A., Holgado, B.L., Wu, X., Wang, X., Parsons, M., Zayne, K., et al. (2018). A Hematogenous Route for Medulloblastoma Leptomeningeal Metastases. Cell *173*, 1549. https://doi.org/10.1016/j.cell.2018.05.033.
9. Li, M., Deng, Y., and Zhang, W. (2021). Molecular Determinants of Medulloblastoma Metastasis and Leptomeningeal Dissemination. Mol. Cancer Res. *19*, 743–752. https://doi.org/10.1158/1541-7786.MCR-20-1026.
10. Van Ommeren, R., Garzia, L., Holgado, B.L., Ramaswamy, V., and Taylor, M.D. (2020). The molecular biology of medulloblastoma metastasis. Brain Pathol. *30*, 691–702. https://doi.org/10.1111/bpa.12811.
11. Grausam, K.B., Dooyema, S.D.R., Bihannic, L., Premathilake, H., Morrissy, A.S., Forget, A., Schaefer, A.M., Gundelach, J.H., Macura, S., Maher, D.M., et al. (2017). ATOH1 Promotes Leptomeningeal Dissemination and Metastasis of Sonic Hedgehog Subgroup Medulloblastomas. Cancer Res. *77*, 3766–3777. https://doi.org/10.1158/0008-5472.CAN-16-1836.
12. Dhall, G. (2009). Medulloblastoma. J. Child Neurol. *24*, 1418–1430. https://doi.org/10.1177/0883073809341668.
13. Remke, M., Ramaswamy, V., and Taylor, M.D. (2013). Medulloblastoma molecular dissection: the way toward targeted therapy. Curr. Opin. Oncol. *25*, 674–681. https://doi.org/10.1097/CCO.0000000000000008.
14. Kool, M., Korshunov, A., Remke, M., Jones, D.T.W., Schlanstein, M., Northcott, P.A., Cho, Y.J., Koster, J., Schouten-van Meeteren, A., van Vuurden, D., et al. (2012). Molecular subgroups of medulloblastoma: an international meta-analysis of transcriptome, genetic aberrations, and clinical data of WNT, SHH, Group 3, and Group 4 medulloblastomas. Acta Neuropathol. *123*, 473–484. https://doi.org/10.1007/s00401-012-0958-8.
15. Miranda Kuzan-Fischer, C., Juraschka, K., and Taylor, M.D. (2018). Medulloblastoma in the Molecular Era. J. Korean Neurosurg. Soc. *61*, 292–301. https://doi.org/10.3340/jkns.2018.0028.
16. Northcott, P.A., Korshunov, A., Pfister, S.M., and Taylor, M.D. (2012). The clinical

implications of medulloblastoma subgroups. Nat. Rev. Neurol. *8*, 340–351. https://doi.org/10.1038/nrneurol.2012.78.
17. Cho, Y.J., Tsherniak, A., Tamayo, P., Santagata, S., Ligon, A., Greulich, H., Berhoukim, R., Amani, V., Goumnerova, L., Eberhart, C.G., et al. (2011). Integrative genomic analysis of medulloblastoma identifies a molecular subgroup that drives poor clinical outcome. J. Clin. Oncol. *29*, 1424–1430. https://doi.org/10.1200/JCO.2010.28.5148.
18. Northcott, P.A., Korshunov, A., Witt, H., Hielscher, T., Eberhart, C.G., Mack, S., Bouffet, E., Clifford, S.C., Hawkins, C.E., French, P., et al. (2011). Medulloblastoma comprises four distinct molecular variants. J. Clin. Oncol. *29*, 1408–1414. https://doi.org/10.1200/JCO.2009.27.4324.
19. Fults, D.W., Taylor, M.D., and Garzia, L. (2019). Leptomeningeal dissemination: a sinister pattern of medulloblastoma growth. J. Neurosurg. Pediatr. *23*, 613–621. https://doi.org/10.3171/2018.11.PEDS18506.
20. Wu, X., Northcott, P.A., Dubuc, A., Dupuy, A.J., Shih, D.J.H., Witt, H., Croul, S., Bouffet, E., Fults, D.W., Eberhart, C.G., et al. (2012). Clonal selection drives genetic divergence of metastatic medulloblastoma. Nature *482*, 529–533. https://doi.org/10.1038/nature10825.
21. Vladoiu, M.C., El-Hamamy, I., Donovan, L.K., Farooq, H., Holgado, B.L., Sundaravadanam, Y., Ramaswamy, V., Hendrikse, L.D., Kumar, S., Mack, S.C., et al. (2019). Childhood cerebellar tumours mirror conserved fetal transcriptional programs. Nature *572*, 67–73. https://doi.org/10.1038/s41586-019-1158-7.
22. Schüller, U., Heine, V.M., Mao, J., Kho, A.T., Dillon, A.K., Han, Y.G., Huillard, E., Sun, T., Ligon, A.H., Qian, Y., et al. (2008). Acquisition of granule neuron precursor identity is a critical determinant of progenitor cell competence to form Shh-induced medulloblastoma. Cancer Cell *14*, 123–134. https://doi.org/10.1016/j.ccr.2008.07.005.
23. Gibson, P., Tong, Y., Robinson, G., Thompson, M.C., Currle, D.S., Eden, C., Kranenburg, T.A., Hogg, T., Poppleton, H., Martin, J., et al. (2010). Subtypes of medulloblastoma have distinct developmental origins. Nature *468*, 1095–1099. https://doi.org/10.1038/nature09587.
24. Oliver, T.G., Read, T.A., Kessler, J.D., Mehmeti, A., Wells, J.F., Huynh, T.T.T., Lin, S.M., and Wechsler-Reya, R.J. (2005). Loss of patched and disruption of granule cell development in a pre-neoplastic stage of medulloblastoma. Development *132*, 2425–2439. https://doi.org/10.1242/dev.01793.
25. Haldipur, P., Millen, K.J., and Aldinger, K.A. (2022). Human Cerebellar Development and Transcriptomics: Implications for Neurodevelopmental Disorders. Annu. Rev. Neurosci. *45*, 515–531. https://doi.org/10.1146/annurev-neuro-111020-091953.
26. Zhao, F., Li, C., Zhou, Q., Qu, P., Wang, B., Wang, X., Zhang, S., Wang, X., Zhao, C., Zhang, J., et al. (2017). Distinctive localization and MRI features correlate of molecular subgroups in adult medulloblastoma. J. Neuro Oncol. *135*, 353–360. https://doi.org/10.1007/s11060-017-2581-y.
27. Wefers, A.K., Warmuth-Metz, M., Pöschl, J., von Bueren, A.O., Monoranu, C.M., Seelos, K., Peraud, A., Tonn, J.C., Koch, A., Pietsch, T., et al. (2014). Subgroup-specific localization of human medulloblastoma based on pre-operative MRI. Acta Neuropathol. *127*, 931–933. https://doi.org/10.1007/s00401-014-1271-5.
28. Perreault, S., Ramaswamy, V., Achrol, A.S., Chao, K., Liu, T.T., Shih, D., Remke, M., Schubert, S., Bouffet, E., Fisher, P.G., et al. (2014). MRI surrogates for molecular subgroups of medulloblastoma. AJNR. Am. J. Neuroradiol. *35*, 1263–1269. https://doi.org/10.3174/ajnr.A3990.
29. Tan, I.L., Wojcinski, A., Rallapalli, H., Lao, Z., Sanghrajka, R.M., Stephen, D., Volkova, E., Korshunov, A., Remke, M., Taylor, M.D., et al. (2018). Lateral cerebellum is preferentially sensitive to high sonic hedgehog signaling and medulloblastoma formation. Proc. Natl. Acad. Sci. USA *115*, 3392–3397. https://doi.org/10.1073/pnas.1717815115.
30. Lewis, P.M., Gritli-Linde, A., Smeyne, R., Kottmann, A., and McMahon, A.P. (2004). Sonic hedgehog signaling is required for expansion of granule neuron precursors and patterning of the mouse cerebellum. Dev. Biol. *270*, 393–410. https://doi.org/10.1016/j.ydbio.2004.03.007.
31. Corrales, J.D., Blaess, S., Mahoney, E.M., and Joyner, A.L. (2006). The level of sonic hedgehog signaling regulates the complexity of cerebellar foliation. Development *133*, 1811–1821. https://doi.org/10.1242/dev.02351.
32. Flora, A., Klisch, T.J., Schuster, G., and Zoghbi, H.Y. (2009). Deletion of Atoh1 disrupts Sonic Hedgehog signaling in the developing cerebellum and prevents medulloblastoma. Science *326*, 1424–1427. https://doi.org/10.1126/science.1181453.
33. Khatua, S. (2016). Evolving molecular era of childhood medulloblastoma: time to revisit therapy. Future Oncol. *12*, 107–117. https://doi.org/10.2217/fon.15.284.
34. Skowron, P., Farooq, H., Cavalli, F.M.G., Morrissy, A.S., Ly, M., Hendrikse, L.D., Wang, E.Y., Djambazian, H., Zhu, H., Mungall, K.L., et al. (2021). The transcriptional landscape of Shh medulloblastoma. Nat. Commun. *12*, 1749. https://doi.org/10.1038/s41467-021-21883-0.
35. Northcott, P.A., Hielscher, T., Dubuc, A., Mack, S., Shih, D., Remke, M., Al-Halabi, H., Albrecht, S., Jabado, N., Eberhart, C.G., et al. (2011). Pediatric and adult sonic hedgehog medulloblastomas are clinically and molecularly distinct. Acta Neuropathol. *122*, 231–240. https://doi.org/10.1007/s00401-011-0846-7.
36. Kool, M., Jones, D.T.W., Jäger, N., Northcott, P.A., Pugh, T.J., Hovestadt, V., Piro, R.M., Esparza, L.A., Markant, S.L., Remke, M., et al. (2014). Genome sequencing of SHH medulloblastoma predicts genotype-related response to smoothened inhibition. Cancer Cell *25*, 393–405. https://doi.org/10.1016/j.ccr.2014.02.004.
37. Northcott, P.A., Buchhalter, I., Morrissy, A.S., Hovestadt, V., Weischenfeldt, J., Ehrenberger, T., Gröbner, S., Segura-Wang, M., Zichner, T., Rudneva, V.A., et al. (2017). The whole-genome landscape of medulloblastoma subtypes. Nature *547*, 311–317. https://doi.org/10.1038/nature22973.
38. Osborn, A.G., Louis, D.N., Poussaint, T.Y., Linscott, L.L., and Salzman, K.L. (2022). The 2021 World Health Organization Classification of Tumors of the Central Nervous System: What Neuroradiologists Need to Know. AJNR. Am. J. Neuroradiol. *43*, 928–937. https://doi.org/10.3174/ajnr.A7462.
39. Archer, T.C., Ehrenberger, T., Mundt, F., Gold, M.P., Krug, K., Mah, C.K., Mahoney, E.L., Daniel, C.J., LeNail, A., Ramamoorthy, D., et al. (2018). Proteomics, Post-translational Modifications, and Integrative Analyses Reveal Molecular Heterogeneity within Medulloblastoma Subgroups. Cancer Cell *34*, 396–410.e8. https://doi.org/10.1016/j.ccell.2018.08.004.
40. Schwalbe, E.C., Lindsey, J.C., Nakjang, S., Crosier, S., Smith, A.J., Hicks, D., Rafiee, G., Hill, R.M., Iliasova, A., Stone, T., et al. (2017). Novel molecular subgroups for clinical classification and outcome prediction in childhood medulloblastoma: a cohort study. Lancet Oncol. *18*, 958–971. https://doi.org/10.1016/S1470-2045(17)30243-7.
41. Cavalli, F.M.G., Remke, M., Rampasek, L., Peacock, J., Shih, D.J.H., Luu, B., Garzia, L., Torchia, J., Nor, C., Morrissy, A.S., et al. (2017). Intertumoral Heterogeneity within Medulloblastoma Subgroups. Cancer Cell *31*, 737–754.e6. https://doi.org/10.1016/j.ccell.2017.05.005.
42. Garcia-Lopez, J., Kumar, R., Smith, K.S., and Northcott, P.A. (2021). Deconstructing Sonic Hedgehog Medulloblastoma: Molecular Subtypes, Drivers, and Beyond. Trends Genet. *37*, 235–250. https://doi.org/10.1016/j.tig.2020.11.001.
43. Parsons, D.W., Li, M., Zhang, X., Jones, S., Leary, R.J., Lin, J.C.H., Boca, S.M., Carter, H., Samayoa, J., Bettegowda, C., et al. (2011). The genetic landscape of the childhood cancer medulloblastoma. Science *331*, 435–439. https://doi.org/10.1126/science.1198056.
44. Rao, R.C., and Dou, Y. (2015). Hijacked in cancer: the KMT2 (MLL) family of methyltransferases. Nat. Rev. Cancer *15*, 334–346. https://doi.org/10.1038/nrc3929.
45. Jones, D.T.W., Jäger, N., Kool, M., Zichner, T., Hutter, B., Sultan, M., Cho, Y.J., Pugh, T.J., Hovestadt, V., Stütz, A.M., et al. (2012). Dissecting the genomic complexity underlying medulloblastoma. Nature *488*, 100–105. https://doi.org/10.1038/nature11284.
46. Pugh, T.J., Weeraratne, S.D., Archer, T.C., Pomeranz Krummel, D.A., Auclair, D., Bochicchio, J., Carneiro, M.O., Carter, S.L., Cibulskis, K., Erlich, R.L., et al. (2012). Medulloblastoma exome sequencing uncovers subtype-specific somatic mutations. Nature *488*, 106–110. https://doi.org/10.1038/nature11329.
47. Guenther, M.G., Levine, S.S., Boyer, L.A., Jaenisch, R., and Young, R.A. (2007). A chromatin landmark and transcription initiation at most promoters in human cells. Cell *130*, 77–88. https://doi.org/10.1016/j.cell.2007.05.042.
48. Froimchuk, E., Carey, S.T., Edwards, C., and Jewell, C.M. (2020). Self-Assembly as a Molecular Strategy to Improve Immunotherapy. Acc. Chem. Res. *53*, 2534–2545. https://doi.org/10.1021/acs.accounts.0c00438.
49. Ang, S.Y., Uebersohn, A., Spencer, C.I., Huang, Y., Lee, J.E., Ge, K., and Bruneau, B.G. (2016). KMT2D regulates specific programs in heart development via histone H3 lysine 4 di-methylation. Development

143, 810–821. https://doi.org/10.1242/dev.132688.

50. Dhar, S.S., Zhao, D., Lin, T., Gu, B., Pal, K., Wu, S.J., Alam, H., Lv, J., Yun, K., Gopalakrishnan, V., et al. (2018). MLL4 Is Required to Maintain Broad H3K4me3 Peaks and Super-Enhancers at Tumor Suppressor Genes. Mol. Cell *70*, 825–841.e6. https://doi.org/10.1016/j.molcel.2018.04.028.
51. Froimchuk, E., Jang, Y., and Ge, K. (2017). Histone H3 lysine 4 methyltransferase KMT2D. Gene *627*, 337–342. https://doi.org/10.1016/j.gene.2017.06.056.
52. Massagué, J. (2012). TGFbeta signalling in context. Nat. Rev. Mol. Cell Biol. *13*, 616–630. https://doi.org/10.1038/nrm3434.
53. Kahn, S.A., Wang, X., Nitta, R.T., Gholamin, S., Theruvath, J., Hutter, G., Azad, T.D., Wadi, L., Bolin, S., Ramaswamy, V., et al. (2018). Notch1 regulates the initiation of metastasis and self-renewal of Group 3 medulloblastoma. Nat. Commun. *9*, 4121. https://doi.org/10.1038/s41467-018-06564-9.
54. Roussel, M.F., and Robinson, G.W. (2013). Role of MYC in Medulloblastoma. Cold Spring Harb. Perspect. Med. *3*, a014308. https://doi.org/10.1101/cshperspect.a014308.
55. Shrestha, S., Morcavallo, A., Gorrini, C., and Chesler, L. (2021). Biological Role of MYCN in Medulloblastoma: Novel Therapeutic Opportunities and Challenges Ahead. Front. Oncol. *11*, 694320. https://doi.org/10.3389/fonc.2021.694320.
56. Vanner, R.J., Remke, M., Gallo, M., Selvadurai, H.J., Coutinho, F., Lee, L., Kushida, M., Head, R., Morrissy, S., Zhu, X., et al. (2014). Quiescent sox2(+) cells drive hierarchical growth and relapse in sonic hedgehog subgroup medulloblastoma. Cancer Cell *26*, 33–47. https://doi.org/10.1016/j.ccr.2014.05.005.
57. Adolphe, C., Millar, A., Kojic, M., Barkauskas, D.S., Sundström, A., Swartling, F.J., Hediyeh-Zadeh, S., Tan, C.W., Davis, M.J., Genovesi, L.A., and Wainwright, B.J. (2021). SOX9 Defines Distinct Populations of Cells in SHH Medulloblastoma but Is Not Required for Math1-Driven Tumor Formation. Mol. Cancer Res. *19*, 1831–1839. https://doi.org/10.1158/1541-7786.MCR-21-0117.
58. Selvadurai, H.J., Luis, E., Desai, K., Lan, X., Vladoiu, M.C., Whitley, O., Galvin, C., Vanner, R.J., Lee, L., Whetstone, H., et al. (2020). Medulloblastoma Arises from the Persistence of a Rare and Transient Sox2(+) Granule Neuron Precursor. Cell Rep. *31*, 107511. https://doi.org/10.1016/j.celrep.2020.03.075.
59. Ahlfeld, J., Favaro, R., Pagella, P., Kretzschmar, H.A., Nicolis, S., and Schüller, U. (2013). Sox2 requirement in sonic hedgehog-associated medulloblastoma. Cancer Res. *73*, 3796–3807. https://doi.org/10.1158/0008-5472.CAN-13-0238.
60. Vong, K.I., Leung, C.K.Y., Behringer, R.R., and Kwan, K.M. (2015). Sox9 is critical for suppression of neurogenesis but not initiation of gliogenesis in the cerebellum. Mol. Brain *8*, 25. https://doi.org/10.1186/s13041-015-0115-0.
61. Cerami, E., Gao, J., Dogrusoz, U., Gross, B.E., Sumer, S.O., Aksoy, B.A., Jacobsen, A., Byrne, C.J., Heuer, M.L., Larsson, E., et al. (2012). The cBio cancer genomics portal: an open platform for exploring multidimensional cancer genomics data. Cancer Discov. *2*, 401–404. https://doi.org/10.1158/2159-8290.CD-12-0095.
62. Gao, J., Aksoy, B.A., Dogrusoz, U., Dresdner, G., Gross, B., Sumer, S.O., Sun, Y., Jacobsen, A., Sinha, R., Larsson, E., et al. (2013). Integrative analysis of complex cancer genomics and clinical profiles using the cBioPortal. Sci. Signal. *6*, pl1. https://doi.org/10.1126/scisignal.2004088.
63. Lee, J.E., Wang, C., Xu, S., Cho, Y.W., Wang, L., Feng, X., Baldridge, A., Sartorelli, V., Zhuang, L., Peng, W., and Ge, K. (2013). H3K4 mono- and di-methyltransferase MLL4 is required for enhancer activation during cell differentiation. Elife *2*, e01503. https://doi.org/10.7554/eLife.01503.
64. Jang, Y., Broun, A., Wang, C., Park, Y.K., Zhuang, L., Lee, J.E., Froimchuk, E., Liu, C., and Ge, K. (2019). H3.3K4M destabilizes enhancer H3K4 methyltransferases MLL3/MLL4 and impairs adipose tissue development. Nucleic Acids Res. *47*, 607–620. https://doi.org/10.1093/nar/gky982.
65. Lawton, A.K., Engstrom, T., Rohrbach, D., Omura, M., Turnbull, D.H., Mamou, J., Zhang, T., Schwarz, J.M., and Joyner, A.L. (2019). Cerebellar folding is initiated by mechanical constraints on a fluid-like layer without a cellular pre-pattern. Elife *8*, e45019. https://doi.org/10.7554/eLife.45019.
66. Matei, V., Pauley, S., Kaing, S., Rowitch, D., Beisel, K.W., Morris, K., Feng, F., Jones, K., Lee, J., and Fritzsch, B. (2005). Smaller inner ear sensory epithelia in Neurog 1 null mice are related to earlier hair cell cycle exit. Dev. Dynam. *234*, 633–650. https://doi.org/10.1002/dvdy.20551.
67. Kawaguchi, Y., Cooper, B., Gannon, M., Ray, M., MacDonald, R.J., and Wright, C.V.E. (2002). The role of the transcriptional regulator Ptf1a in converting intestinal to pancreatic progenitors. Nat. Genet. *32*, 128–134. https://doi.org/10.1038/ng959.
68. Zhuo, L., Theis, M., Alvarez-Maya, I., Brenner, M., Willecke, K., and Messing, A. (2001). hGFAP-cre transgenic mice for manipulation of glial and neuronal function *in vivo*. Genesis *31*, 85–94. https://doi.org/10.1002/gene.10008.
69. Lao, Z., Raju, G.P., Bai, C.B., and Joyner, A.L. (2012). MASTR: a technique for mosaic mutant analysis with spatial and temporal control of recombination using conditional floxed alleles in mice. Cell Rep. *2*, 386–396. https://doi.org/10.1016/j.celrep.2012.07.004.
70. Yan, X., Liu, Z., and Chen, Y. (2009). Regulation of TGF-beta signaling by Smad7. Acta Biochim. Biophys. Sin. *41*, 263–272. https://doi.org/10.1093/abbs/gmp018.
71. Ying, M., Sang, Y., Li, Y., Guerrero-Cazares, H., Quinones-Hinojosa, A., Vescovi, A.L., Eberhart, C.G., Xia, S., and Laterra, J. (2011). Kruppel-like family of transcription factor 9, a differentiation-associated transcription factor, suppresses Notch1 signaling and inhibits glioblastoma-initiating stem cells. Stem Cell. *29*, 20–31. https://doi.org/10.1002/stem.561.
72. Ying, M., Tilghman, J., Wei, Y., Guerrero-Cazares, H., Quinones-Hinojosa, A., Ji, H., and Laterra, J. (2014). Kruppel-like factor-9 (KLF9) inhibits glioblastoma stemness through global transcription repression and integrin alpha6 inhibition. J. Biol. Chem. *289*, 32742–32756. https://doi.org/10.1074/jbc.M114.588988.
73. Sarić, N., Selby, M., Ramaswamy, V., Kool, M., Stockinger, B., Hogstrand, C., Williamson, D., Marino, S., Taylor, M.D., Clifford, S.C., and Basson, M.A. (2020). The AHR pathway represses TGFbeta-SMAD3 signalling and has a potent tumour suppressive role in SHH medulloblastoma. Sci. Rep. *10*, 148. https://doi.org/10.1038/s41598-019-56876-z.
74. Morabito, M., Larcher, M., Cavalli, F.M., Foray, C., Forget, A., Mirabal-Ortega, L., Andrianteranagna, M., Druillennec, S., Garancher, A., Masliah-Planchon, J., et al. (2019). An autocrine ActivinB mechanism drives TGFbeta/Activin signaling in Group 3 medulloblastoma. EMBO Mol. Med. *11*, e9830. https://doi.org/10.15252/emmm.201809830.
75. Adachi, T., Miyashita, S., Yamashita, M., Shimoda, M., Okonechnikov, K., Chavez, L., Kool, M., Pfister, S.M., Inoue, T., Kawauchi, D., and Hoshino, M. (2021). Notch Signaling between Cerebellar Granule Cell Progenitors. eNeuro *8*. ENEURO.0468-20.2021. https://doi.org/10.1523/ENEURO.0468-20.2021.
76. Natarajan, S., Li, Y., Miller, E.E., Shih, D.J., Taylor, M.D., Stearns, T.M., Bronson, R.T., Ackerman, S.L., Yoon, J.K., and Yun, K. (2013). Notch1-induced brain tumor models the sonic hedgehog subgroup of human medulloblastoma. Cancer Res. *73*, 5381–5390. https://doi.org/10.1158/0008-5472.CAN-13-0033.
77. Wei, L., Shao, N., Peng, Y., and Zhou, P. (2021). Inhibition of Cathepsin S Restores TGF-beta-induced Epithelial-to-mesenchymal Transition and Tight Junction Turnover in Glioblastoma Cells. J. Cancer *12*, 1592–1603. https://doi.org/10.7150/jca.50631.
78. Zhang, L.Y., Guo, Q., Guan, G.F., Cheng, W., Cheng, P., and Wu, A.H. (2019). Integrin Beta 5 Is a Prognostic Biomarker and Potential Therapeutic Target in Glioblastoma. Front. Oncol. *9*, 904. https://doi.org/10.3389/fonc.2019.00904.
79. Kunigal, S., Gondi, C.S., Gujrati, M., Lakka, S.S., Dinh, D.H., Olivero, W.C., and Rao, J.S. (2006). SPARC-induced migration of glioblastoma cell lines via uPA-uPAR signaling and activation of small GTPase RhoA. Int. J. Oncol. *29*, 1349–1357. https://www.ncbi.nlm.nih.gov/pubmed/17088972.
80. Karki, K., Li, X., Jin, U.H., Mohankumar, K., Zarei, M., Michelhaugh, S.K., Mittal, S., Tjalkens, R., and Safe, S. (2020). Nuclear receptor 4A2 (NR4A2) is a druggable target for glioblastomas. J. Neuro Oncol. *146*, 25–39. https://doi.org/10.1007/s11060-019-03349-y.
81. Koso, H., Tsuhako, A., Lyons, E., Ward, J.M., Rust, A.G., Adams, D.J., Jenkins, N.A., Copeland, N.G., and Watanabe, S. (2014). Identification of FoxR2 as an oncogene in medulloblastoma. Cancer Res. *74*, 2351–2361. https://doi.org/10.1158/0008-5472.CAN-13-1523.
82. Mumert, M., Dubuc, A., Wu, X., Northcott, P.A., Chin, S.S., Pedone, C.A., Taylor, M.D., and Fults, D.W. (2012). Functional genomics identifies drivers of medulloblastoma dissemination. Cancer Res. *72*, 4944–4953. https://doi.org/10.1158/0008-5472.CAN-12-1629.
83. Jenkins, N.C., Kalra, R.R., Dubuc, A., Sivakumar, W., Pedone, C.A., Wu, X., Taylor,

M.D., and Fults, D.W. (2014). Genetic drivers of metastatic dissemination in sonic hedgehog medulloblastoma. Acta Neuropathol. Commun. *2*, 85. https://doi.org/10.1186/s40478-014-0085-y.

84. Tsai, Y.P., and Wu, K.J. (2012). Hypoxia-regulated target genes implicated in tumor metastasis. J. Biomed. Sci. *19*, 102. https://doi.org/10.1186/1423-0127-19-102.
85. Chi, Y., Remsik, J., Kiseliovas, V., Derderian, C., Sener, U., Alghader, M., Saadeh, F., Nikishina, K., Bale, T., Iacobuzio-Donahue, C., et al. (2020). Cancer cells deploy lipocalin-2 to collect limiting iron in leptomeningeal metastasis. Science *369*, 276–282. https://doi.org/10.1126/science.aaz2193.
86. Vengellur, A., Woods, B.G., Ryan, H.E., Johnson, R.S., and LaPres, J.J. (2003). Gene expression profiling of the hypoxia signaling pathway in hypoxia-inducible factor 1alpha null mouse embryonic fibroblasts. Gene Expr. *11*, 181–197. https://doi.org/10.3727/000000003108749062.
87. Wang, X., Dubuc, A.M., Ramaswamy, V., Mack, S., Gendoo, D.M.A., Remke, M., Wu, X., Garzia, L., Luu, B., Cavalli, F., et al. (2015). Medulloblastoma subgroups remain stable across primary and metastatic compartments. Acta Neuropathol. *129*, 449–457. https://doi.org/10.1007/s00401-015-1389-0.
88. Jenkins, N.C., Rao, G., Eberhart, C.G., Pedone, C.A., Dubuc, A.M., and Fults, D.W. (2016). Somatic cell transfer of c-Myc and Bcl-2 induces large-cell anaplastic medulloblastomas in mice. J. Neuro Oncol. *126*, 415–424. https://doi.org/10.1007/s11060-015-1985-9.
89. Kawauchi, D., Robinson, G., Uziel, T., Gibson, P., Rehg, J., Gao, C., Finkelstein, D., Qu, C., Pounds, S., Ellison, D.W., et al. (2012). A mouse model of the most aggressive subgroup of human medulloblastoma. Cancer Cell *21*, 168–180. https://doi.org/10.1016/j.ccr.2011.12.023.
90. Niesen, J., Ohli, J., Sedlacik, J., Dührsen, L., Hellwig, M., Spohn, M., Holsten, T., and Schüller, U. (2020). Pik3ca mutations significantly enhance the growth of SHH medulloblastoma and lead to metastatic tumour growth in a novel mouse model. Cancer Lett. *477*, 10–18. https://doi.org/10.1016/j.canlet.2020.02.028.
91. Tronche, F., Kellendonk, C., Kretz, O., Gass, P., Anlag, K., Orban, P.C., Bock, R., Klein, R., and Schütz, G. (1999). Disruption of the glucocorticoid receptor gene in the nervous system results in reduced anxiety. Nat. Genet. *23*, 99–103. https://doi.org/10.1038/12703.
92. Giusti, S.A., Vercelli, C.A., Vogl, A.M., Kolarz, A.W., Pino, N.S., Deussing, J.M., and Refojo, D. (2014). Behavioral phenotyping of Nestin-Cre mice: implications for genetic mouse models of psychiatric disorders. J. Psychiatr. Res. *55*, 87–95. https://doi.org/10.1016/j.jpsychires.2014.04.002.
93. Wojcinski, A., Morabito, M., Lawton, A.K., Stephen, D.N., and Joyner, A.L. (2019). Genetic deletion of genes in the cerebellar rhombic lip lineage can stimulate compensation through adaptive reprogramming of ventricular zone-derived progenitors. Neural Dev. *14*, 4. https://doi.org/10.1186/s13064-019-0128-y.
94. Mao, J., Ligon, K.L., Rakhlin, E.Y., Thayer, S.P., Bronson, R.T., Rowitch, D., and McMahon, A.P. (2006). A novel somatic mouse model to survey tumorigenic potential applied to the Hedgehog pathway. Cancer Res. *66*, 10171–10178. https://doi.org/10.1158/0008-5472.CAN-06-0657.
95. Ellis, T., Smyth, I., Riley, E., Graham, S., Elliot, K., Narang, M., Kay, G.F., Wicking, C., and Wainwright, B. (2003). Patched 1 conditional null allele in mice. Genesis *36*, 158–161. https://doi.org/10.1002/gene.10208.
96. Schneider, C.A., Rasband, W.S., and Eliceiri, K.W. (2012). NIH Image to ImageJ: 25 years of image analysis. Nat. Methods *9*, 671–675. https://doi.org/10.1038/nmeth.2089.
97. Love, M.I., Huber, W., and Anders, S. (2014). Moderated estimation of fold change and dispersion for RNA-seq data with DESeq2. Genome Biol. *15*, 550. https://doi.org/10.1186/s13059-014-0550-8.
98. Zhang, Y., Liu, T., Meyer, C.A., Eeckhoute, J., Johnson, D.S., Bernstein, B.E., Nusbaum, C., Myers, R.M., Brown, M., Li, W., and Liu, X.S. (2008). Model-based analysis of ChIP-Seq (MACS). Genome Biol. *9*, R137. https://doi.org/10.1186/gb-2008-9-9-r137.
99. Quinlan, A.R., and Hall, I.M. (2010). BEDTools: a flexible suite of utilities for comparing genomic features. Bioinformatics *26*, 841–842. https://doi.org/10.1093/bioinformatics/btq033.
100. Heinz, S., Benner, C., Spann, N., Bertolino, E., Lin, Y.C., Laslo, P., Cheng, J.X., Murre, C., Singh, H., and Glass, C.K. (2010). Simple combinations of lineage-determining transcription factors prime cis-regulatory elements required for macrophage and B cell identities. Mol. Cell *38*, 576–589. https://doi.org/10.1016/j.molcel.2010.05.004.
101. Ramírez, F., Dündar, F., Diehl, S., Grüning, B.A., and Manke, T. (2014). deepTools: a flexible platform for exploring deep-sequencing data. Nucleic Acids Res. *42*, W187–W191. https://doi.org/10.1093/nar/gku365.
102. Chi, J., Crane, A., Wu, Z., and Cohen, P. (2018). Adipo-Clear: A Tissue Clearing Method for Three-Dimensional Imaging of Adipose Tissue. J. Vis. Exp. *137*, 58271. https://doi.org/10.3791/58271.
103. Blaess, S., Bodea, G.O., Kabanova, A., Chanet, S., Mugniery, E., Derouiche, A., Stephen, D., and Joyner, A.L. (2011). Temporal-spatial changes in Sonic Hedgehog expression and signaling reveal different potentials of ventral mesencephalic progenitors to populate distinct ventral midbrain nuclei. Neural Dev. *6*, 29. https://doi.org/10.1186/1749-8104-6-29.
104. Buenrostro, J.D., Giresi, P.G., Zaba, L.C., Chang, H.Y., and Greenleaf, W.J. (2013). Transposition of native chromatin for fast and sensitive epigenomic profiling of open chromatin, DNA-binding proteins and nucleosome position. Nat. Methods *10*, 1213–1218. https://doi.org/10.1038/nmeth.2688.
105. Buenrostro, J.D., Wu, B., Chang, H.Y., and Greenleaf, W.J. (2015). ATAC-seq: A Method for Assaying Chromatin Accessibility Genome-Wide. Curr. Protoc. Mol. Biol. *109*, 21.29.1–21.29.9. https://doi.org/10.1002/0471142727.mb2129s109.
106. Corces, M.R., Trevino, A.E., Hamilton, E.G., Greenside, P.G., Sinnott-Armstrong, N.A., Vesuna, S., Satpathy, A.T., Rubin, A.J., Montine, K.S., Wu, B., et al. (2017). An improved ATAC-seq protocol reduces background and enables interrogation of frozen tissues. Nat. Methods *14*, 959–962. https://doi.org/10.1038/nmeth.4396.

STAR★METHODS

KEY RESOURCES TABLE

REAGENT or RESOURCE	SOURCE	IDENTIFIER
Antibodies		
Mouse Monoclonal anti-Calbindin D-28K	Swant	300
Mouse Monocloanl anti-NeuN	EMD Millipore	MAB377
Mouse Monoclonal anti-p27	Thermo Fisher Scientific	610241
Purified Mouse anti-Ki-67	BD Pharmingen	556003
Mouse Monoclonal anti-NeurodD1	Abcam	ab60704
Rabbit Polyclonal anti-PH3	EMD Millipore	06–570
Donkey anti-Mouse 488 IgG, Alexa Fluor	Invitrogen	A-21202
Donkey anti-Mouse 647 IgG, Alexa Fluor	Invitrogen	A-31571
Donkey Anti-Rabbit IgG, Alexa Fluor 555	Invitrogen	A-31572
Chicken Polyclonal anti-GFP	Aves Lab	GFP-1010
Goat Anti-Chicken 647 IgG, Alexa Fluor	Invitrogen	A-21449
Yoyo1 Iodide (491/509)	Thermo Fisher Scientific	Y3601
Streptavidin Alexa Fluor 647 Conjugate	Invitrogen	S-32357
Click-iT™ EdU Cell Proliferation Kit for Imaging, Alexa Fluor™ 647 dye	Invitrogen	C10340
Click-it EdU assay with Sulfo-Cyanine5 azide	Lumiprobe Corporation	A3330
Rabbit Monoclonal Histone H3 (D1H2)	Cell Signaling Technology	4499
Rabbit Monoclonal H3K4me1 (D1A9)	Cell Signaling Technology	5326p
Rabbit Monoclonal H3K4me3 (C42D8)	Cell Signaling Technology	9751s
Goat Anti-Rabbit Cross-Adsorbed Secondary Antibody, HRP	Thermo Fisher Scientific	G-21234
Thermo Scientific Richard-Allan, Eosin-Y Stain	Thermo Fisher Scientific	22-050-110
Thermo Scientific Richard-Allan, Hematoxylin 2	Thermo Fisher Scientific	22-050-201
Hoechst 33258 (bis-Benzimide)	Thermo Fisher Scientific	H3569
Chemicals, peptides, and recombinant proteins		
Tagment DNA Enzyme 1 (TDE1)	Illumina	15027865
Tagment DNA Buffer	Illumina	15027866
Qiagen MinElute Reaction Cleanup Kit	Qiagen	28204
NEBNext High-Fidelity 2X PCR Master Mix	NEB	M0541S
SYBR Green I	Thermo Fisher Scientific	S7563
Agencourt AMPure XP magnetic beads	Beckman Coulter	A63880
Agilent High Sensitivity DNA Bioanalysis Kit	Agilent Technologies	5067–4626
Qubit dsDNA HS Assay Kit	Thermo Fisher Scientific	Q32851
Tamoxifen	Sigma Aldrich	T5648-1G
BSA	Sigma Aldrich	A2153-100G
EGTA	Sigma Aldrich	E0396
Sodium Dodecyl Sulfate	Thermo Fisher Scientific	BP166-100
Triton X-100	Thermo Fisher Scientific	BP151-100
NP-40 10%	Sigma/Roche	11332473001
Tween-20	Sigma/Roche	11332465001
Digitonin	Promega	G9441

(*Continued on next page*)

Continued

REAGENT or RESOURCE	SOURCE	IDENTIFIER
Biotin-16-dUTP	Sigma Aldrich	11093070910
Terminal Transferase	Roche	3333574001
EdU	Invitrogen	E10187
Mounting, Cryo-OCT	VWR	25608-930
10% SDS	Thermo Fisher Scientific	NP0002
20% Glycerol	Sigma Aldrich	G1724
Protease/phosphatase inhibitor	Thermo Fisher Scientific	78440
4X Loading Buffer	Thermo Fisher Scientific	LDS0007
SeeBlue Plus2 Pre-stained Protein Standard	Invitrogen	LC5925
MES SDS running buffer	Thermo Fisher Scientific	NP0002
NUPAGE 20X Transfer Buffer	Thermo Fisher Scientific	NP0006-1
NUPAGE Antioxidant	Thermo Fisher Scientific	NP0005
NuPAGE™ 12%, Bis-Tris, 1.0 mm, Mini Protein Gels	Thermo Fisher Scientific	NP0341PK2
Thermo Scientific Pierce ECL Western Blotting Substrate	Thermo Fisher Scientific	32106
Dichloromethane	Sigma Aldrich	270997-100ML
Dibenzyl ether (98%)	Sigma Aldrich	108014-1KG
Critical commercial assays		
Rneasy Plus Mini Kit	Qiagen	74134
iScript cDNA Synthesis Kit	Bio-Rad	170-8891
Papain Dissociation System	Worthington Biochemical Corporation	LK003150
Deposited data		
Raw and analyzed data	This paper	GEO: GSE211030
Experimental models: Organisms/strains		
Nestin-Cre	The Jackson Laboratory Tronche et al.,[91] Giusti et al.[92]	Strain #003771
Atoh1-Cre	Matei et al.[66]	Strain #011104
hGFAP-Cre	Zhuo et al.[68]	Strain #004600
Ptf1a^{Cre}	Kawaguchi et al.[67]	MGI:2387804
Kmt2d$^{Cf/Cf}$ or *Kmt2d*$^{(Exon50-51)flox/flox}$	Jang et al.[64]	
Kmt2d$^{Nf/Nf}$ or *Kmt2d*$^{(Exon16-19)flox/flox}$	Lee et al.[63]	Strain #032152
Atoh1-FlpoER/+	Wojcinski et al.,[93]	Available through the Joyner Lab
R26$^{LSL-eGFP-Cre}$	Lao et al.[69]	Strain 019013
R26$^{LSL-SmoM2-Yfp}$	The Jackson Laboratory Mao et al.[94]	Strain #005130
Ptch1$^{fl/fl}$	The Jackson Laboratory Ellis et al.[95]	Strain #030494
Oligonucleotides		
Kcnc3 Forward: ACCCAACTACTGCAAGCCTGAC *Kcnc3* Reverse: CACTTGTCCTTTCTGTCTGCTG	Allen Brain atlas	*In situ* hybridization
Myc Forward: GTCCGAGTGCATTGACCC *Myc* Reverse: TACAGTCCCAAAGCCCCA	Allen Brain atlas	*In situ* hybridization
Gapdh Forward: AGGTCGGTGTGAACGGATTTG *Gapdh* Reverse: TGTAGACCATGTAGTTGAGGTCA	IDT DNA	qPCR
Atoh1 Forward: GGTCTGTGGTGATCGTTGTTA *Atoh1* Reverse: TACAGAGGAAGGAGAAGGTAGG	IDT DNA	qPCR

(*Continued on next page*)

Continued

REAGENT or RESOURCE	SOURCE	IDENTIFIER
Sox2 Forward: CAGGAGTTGTCAAGGCAGAG *Sox2* Reverse: GCTCCAAACTTCTCTCCTTTCT	IDT DNA	qPCR
Myc Forward: CGCCTACATCCTGTCCATTC *Myc* Reverse: AAGCTGTTCGAGTTTGTGTTTC	IDT DNA	qPCR
NeuroD1 Forward: AGGCACGTCAGTTTCACTATTC *NeuroD1* Reverse: GCACTTTGCAGCAATCTTAGC	IDT DNA	qPCR
Jag1 Forward: ATGGGTCAGAACTGTGACATAAA *Jag1* Reverse: GGTGGACAGATACAGCGATAAC	IDT DNA	qPCR
Hes1 Forward: CCAGCCAGTGTCAACACGA *Hes1* Reverse: AATGCCGGGAGCTATCTTTCT	IDT DNA	qPCR
Klf9 Forward: TAGGTTAGGCTGCCCATTTC *Klf9* Reverse: CCCAAACTCCTCACTCACTAAA	IDT DNA	qPCR
Tgfbr2 Forward: GTTCGTGAGCATGGAGAGATAG *Tgfbr2* Reverse: CAGGGCTGAGATGATAAGAGTG	IDT DNA	qPCR
Smad3 Forward: CACGCAGAACGTGAACACC *Smad3* Reverse: GGCAGTAGATAACGTGAGGGA	IDT DNA	qPCR
Smad7 Forward: GCCCTCCCTGGATATCTTCTAT *Smad7* Reverse: GATCTTGCTCCGCACTTTCT	IDT DNA	qPCR
Software and algorithms		
ImageJ	Schneider et al.[96]	https://ImageJ.nih.gov/ij/
DESeq2	Love et al.[97]	https://bioconductor.org/packages/release/bioc/html/DESeq2.html
MACS2	Zhang et al.[98]	https://github.com/macs3-project/MACS
BEDTools	Quinlan et al.[99]	http://bedtools.readthedocs.io
Homer	Heinz et al.[100]	http://homer.ucsd.edu/
deepTools	Ramírez et al.[101]	https://deeptools.readthedocs.io/en/develop/
Graphpad Prism	GraphPad	www.graphpad.com

RESOURCE AVAILABILITY

Lead contact

Further information and requests for resources and reagents should be directed to and will be fulfilled by the lead contact, Dr. Alexandra L. Joyner (joynera@mskcc.org).

Materials availability

This study did not generate new unique reagents.

Data and code availability

- All sequencing data have been deposited at GEO and are publicly available as of the date of the publication. The accession code is listed in the key resources table.
- This paper does not report original code.
- Any additional information required to reanalyze data reported in this paper is available from the lead contact upon request.

EXPERIMENTAL MODEL AND STUDY PARTICIPANT DETAILS

Animal work and breeding

All animal experiments were performed with the approval of the Institutional Animal Care and Use Committees at Memorial Sloan Kettering Cancer Center. The following mouse lines were used: *Atoh1-Cre*,[66] *Atoh1-FlpoER*,[93] *Rosa26*^{MASTR}(*R26*$^{frt\text{-}STOP\text{-}frt\text{-}GFPcre}$),[69] *R26*$^{LSL\text{-}SmoM2\text{-}YFP}$,[94] *Ptch1*$^{flox/flox}$,[95] *Ptf1a*^{Cre},[67] *hGFAP-Cre*,[68] *Nestin-Cre*,[91,92] *Kmt2d*$^{Cf/Cf}$ or *Kmt2d*$^{(Exon50\text{-}51)flox/flox}$,[64] *Kmt2d*$^{Nf/Nf}$ or *Kmt2d*$^{(Exon16\text{-}19)flox/flox}$.[63] All mouse lines were maintained on an outbred Swiss Webster background, except *R26*$^{LSL\text{-}SmoM2\text{-}YFP}$ which was maintained on a C57BL/6 inbred

background. Both sexes were used for the analysis. Animals were housed on a 12 hr light/dark cycle and were given access to food and water *ad libitum*. All experiments were performed using mice from embryonic stages to adult (ages E18–P300).

Animals for tumor studies were bred to have littermates that were either homozygous and heterozygous for the *Kmt2d* floxed allele or heterozygous and wild type for a *Kmt2d* floxed allele. For example, *Atoh1-FlpoER/+; R26*$^{SmoM2/SmoM2}$*; Kmt2d*$^{Cf/+}$ male mice were bred with *R26*$^{MASTR/+}$*; Kmt2d*$^{Cf/Cf}$ females and *Atoh1-FlpoER/+; R26*$^{SmoM2/SmoM2}$ male mice were bred with *R26*$^{MASTR/MASTR}$*; Kmt2d*$^{Cf/+}$ females or *Atoh1-FlpoER/+; Ptch1*$^{flox/flox}$*; Kmt2d*$^{Cf/+}$ male mice were bred with *R26*$^{MASTR/+}$*; Kmt2d*$^{Cf/CF}$*; Ptch1*$^{flox/flox}$ females and *Atoh1-FlpoER/+; Ptch1*$^{flox/flox}$ male mice were bred with *R26*$^{MASTR/+}$*; Kmt2d*$^{Cf/+}$*; Ptch1*$^{flox/flox}$ females. Animals for developmental studies were bred to have animals with no *Cre* or heterozygous and homozygous conditional mutants all from the same litter. The breeding schemes are described in the key resources table.

To induce genetic recombination using FlpoER, one 200ug/g dose of Tamoxifen (Tm) (Sigma-Aldrich) was injected subcutaneously into the back of P2 mice. Tm was dissolved and stored in corn oil (Sigma-Aldrich) at 20 mg/mL.

METHOD DETAILS

Tissue processing

E18 animals were collected after euthanizing the pregnant mouse by cervical dislocation after they were deeply anesthetized by inhalation of carbon dioxide and brains from embryos were harvested and fixed in 4% paraformaldehyde for 24-48 hr at 4°C. P4 animals were euthanized by decapitation and tissue harvested and fixed in 4% paraformaldehyde for 24-48 hr at 4°C. Animals P12-P300 were anesthetized and transcardially perfused with PBS followed by cold 4% paraformaldehyde (PFA). The brains and spinal cords with the vertebral column intact were dissected and post-fixed in 4% PFA at 4°C separately for 48 hr or overnight, respectively. Brains were then cryoprotected in 30% sucrose before freezing in Cryo-OCT. Frozen brains were sectioned in the sagittal plane at 14 μm. Micro-scissors were used to remove the spinal cords from the vertebral column and fixed in 4% PFA for another 24 hr and then cryoprotected in 30% sucrose before freezing in Cryo-OCT. Frozen spinal cords were coronally sectioned at 20 μm.

Microscopy

Images were collected either on a NanoZoomer 2.0 HT slide scanner (Hamamatsu Photonics) with a 20x objective using NDP.scan software or on a DM6000 Leica microscope using Zen software (Zeiss) using a 20x objective or on a Zeiss LSM 880 confocal microscope system with a 40X objective using Zen software. All images were processed using NDP.view2 or ImageJ Fiji software.[96] 3-dimensional images of spinal cord tumors were collected on a LCS SPIM Light Sheet Microscope from Luxendo with a 20x objective and processed using Imaris Software.

Histology, Immunofluorescence and Immunohistochemistry

To analyze the histopathology of brain and spinal cord tumors, sections were stained with Hematoxylin and Eosin (Thermo Fisher Scientific) (H&E) according to the protocol from the manufacturer. Images were collected on a Nanozoomer 2.0 HT slide scanner.

For immunohistochemical (IHC) analysis sections were blocked for at least 1 hr in 5% BSA (Sigma-Aldrich) and 0.3% Triton X-100 (Fischer Scientific) and incubated overnight at 4°C in antibody diluted in a blocking solution as described in the key resources table. Rabbit anti-PH3, Mouse anti-Ki67, Mouse anti-p27, Alexa fluor 555 Mouse anti-Ki-67, Mouse anti-NeurodD1 and Mouse anti-NeuN required a 40-minute incubation in antigen retrieval solution (10mM Sodium Citrate, 0.05% Tween-20, pH 6.0) at 95°C prior to blocking. Sections were then incubated with a species-specific secondary antibody for 2 hr at room temperature (RT) as described in the key resources table. Nuclei were counterstained with Hoechst 33258 (Invitrogen). Images were collected on a DM6000 Leica microscope or Nanozoomer 2.0 HT slide scanner.

TUNEL staining

Slides were permeabilized with 0.5% TritonX-100, and pre-incubated with Tdt buffer (30 mM Tris·HCl, 140 mM sodium cacodylate and 1 mM $CoCl_2$) for 15 min at RT. Slides were then incubated for 1 hr at 37°C in a TUNEL reaction solution containing Terminal Transferase (Roche) and Biotin-16-dUTP (Sigma-Aldrich), following which slides were incubated with a Streptavidin Alexa Fluor 647 conjugate (Invitrogen S-32357) for 1 hr.

EdU (5-ethynyl-2′-deoxyuridine) Injection and staining

To assess cell proliferation, EdU (Invitrogen) was injected intraperitoneally at 100 mg/g 1 hr before euthanasia. A Click-it EdU assay (Invitrogen C10340) with Sulfo-Cyanine5 azide (Lumiprobe Corporation A3330) was used per the manufacturer's protocol to stain sections.

Clearing and light sheet imaging

To image and construct a 3-dimensional map of a tumor along the spinal cord of a *SmoM2-Kmt2d*$^{Cf/Cf}$ animal, the spinal cord was macrodissected and cleared using an adaptation of the Adipo-Clear method from Dr. ZhuHao Wu.[102] Briefly, samples were post-fixed in 4% PFA overnight at 4°C, dehydrated in a methanol series and delipidated in dichloromethane (DCM) before rehydration in a methanol series. The spinal cords were stained with a primary and secondary antibody for GFP+ tumor cells and a Yoyo1 dye for nuclei as described in the key

resources table for 5 days each. Samples were then fixed in 4% PFA at 4°C, dehydrated through a methanol series and cleared using dibenzylether (DBE). Imaging was done on a LCS SPIM Light sheet microscope from Luxendo with a 20x objective.

RNA *in situ* hybridization

RNA *in situ* hybridization was performed as described in Blaess et al.[103] using antisense RNA probes for *Kcnc3* and *Myc*. The templates for *Kcnc3* and *Myc* were generated by PCR using primers containing T7 or SP6 polymerase promoters from postnatal cerebellum cDNA. The sequences for the primer pairs used to generate probes are listed in the key resources table.

qRT-PCR analysis of GFP+ tumor cell RNA

Approximately 3 million GFP+ cells from *SmoM2* and *SmoM2-Kmt2d*$^{Cf/Cf}$ tumors were sorted and frozen in TRI-reagent (Sigma-Aldrich) from tumor-bearing animals of ages P35-P50. Total RNA was extracted using the mRNeasy kit (Qiagen), and cDNA was synthesized using SuperScript IV reverse transcriptase (Invitrogen). For the real-time PCR, 20ng of cDNA was used per reaction and amplified using StepOnePlus™ Real-Time PCR System. The reactions were using a Step One Plus apparatus and software. The fold change was determined using the formula $2^{-\Delta\Delta CT}$, where ΔΔCT= ΔCT sample – Mean(ΔCT control) with ΔCT= CT gene-CT GAPDH. Statistics were determined using the Mann-Whitney test. Sequence of primer pairs used are listed in the key resources table.

Western Blot

Whole tumor tissue from *SmoM2*, *SmoM2-Kmt2d*$^{Cf/+}$ and *SmoM2-Kmt2d*$^{Cf/Cf}$ animals were snap frozen using 2-methyl butane and dry-ice. Samples were stored at -80°C until ready for protein extraction. Total protein was extracted by sonicating the cells in the appropriate amount of 2x Laemmeli Buffer (4% SDS, 100mM Tris-HCl, pH 6.8, 4% Glycerol, 200mM DTT, with DNase and Protease/Phosphatase inhibitors (Thermo Fischer Scientific) on ice for 30 min. Samples were spun down for 10 minutes at 16,000g and the pellet resuspended in NuPAGE LDS sample buffer (Thermo Fisher Scientific) before protein concentration determination. Samples were run on a 12% Bis-Tris Protein Gel, transferred onto PVDF membranes, stained with primary antibodies for Histone H3, H3K4me1 and H3K4me3 over night at 4°C, followed by species-specific secondary antibodies for 2 hrs. at room temperature all described in the key resources table. ECL Western Blotting Substrate (Thermo Fisher Scientific) was used to develop the membrane. H3K4me1/3 signal intensity was normalized to the signal intensity of Histone H3. Protein content was measured using ImageJ[96] to measure the signal intensity in the appropriate protein band from 3 cell protein samples of each of the 3 genotypes and the intensity reported relative to the average of *SmoM2* tumors.

Sample preparation for sequencing experiments

SmoM2 animals between 6-16 weeks, and *SmoM2-Kmt2d*$^{Cf/+}$ and *SmoM2-Kmt2d*$^{Cf/Cf}$ animals between 5-8 weeks were used for sequencing experiments. The tumor tissue of the brain was macro-dissected from the surrounding normal brain tissue, dissociated and processed using a Papain Kit (Worthington Biochemical Corporation) and the manufacturer's protocol. The GFP+ tumor cells were isolated by fluorescence activated cell sorting in the MSKCC Flow Cytometry Core. From each sample 70,000 cells were processed for ATAC-seq, and 1-5 million cells were frozen at -80°C for RNA-seq.

The spinal cords from the same *SmoM2-Kmt2d*$^{Cf/Cf}$ animals were dissected and dissociated using a papain kit. The GFP+ metastatic tumor cells were isolated by FACS at the MSKCC Flow Cytometry Core. 70,000 cells were processed for ATAC-seq, and 100,000-3 million cells were frozen at 80°C for RNA-seq. Note, the proportion of tumor cells in the spinal cord samples was much lower than in the brain samples for primary tumors, thus contamination with spinal cord cells and immune cells is more likely in the spinal cord samples than primary tumor samples.

RNA-seq sample preparation

Frozen cell pellets of 100,000-3,000,000 cells from spinal cord metastatic tumors and 1-5 million cells from primary brain tumors prepared as described above were submitted to the MSKCC Integrated Genomics Operations (IGO) Core facility for RNA isolation and sequencing.

ATAC-seq sample preparation

DNA was isolated from the sorted GFP+ cells describe above and prepared according to the Omni-ATAC protocol.[104–106] Briefly, 70,000 cells per sample were lysed using 0.1% NP-40, 0.1% Tween and 0.01% Digitonin to yield nuclei. The resulting chromatin was fragmented and tagmented using Tn5 transposase. DNA was purified using a Qiagen MinElute Reaction Cleanup Kit (Qiagen) and amplified using a NEBNext 2x MasterMix (NEB). Libraries were prepared using universal forward and reverse primers from Ad2.1-Ad2.24.[104] The final libraries were purified using a single left-handed bead purification with AMPure beads (Beckman Coulter). Libraries were sent to the MSKCC IGO Core Facility for sequencing.

QUANTIFICATION AND STATISTICAL ANALYSIS

E18.5 GCP proliferation rate, P12/21 TUNEL, KI67, NeuroD1 and EdU quantification

Proliferation rate was determined by quantifying the number of PH3+ cells per area of the outer EGL (mm^2) using the ImageJ software[96] on images collected on the NanoZoomer 2.0 HT slide scanner with a 20x objective. 3 near adjacent hemisphere sections were selected from 3 mice per genotype to manually quantify the number of PH3+ cells and the area of the outer and total EGL.

TUNEL images were taken on a Nanozoomer2.0 HT slide scanner and exported at 20x. Quantification of the TUNEL+ cells on P12 preneoplastic lesions/EGL were performed using ImageJ Fiji Software.[96] Similar fields between the paramedian and copula pyramis lobules in the lateral posterior hemispheres of 3 near adjacent sections were selected and the areas of the EGL (mm^2) manually measured. The quantification of the TUNEL+ particles within that area was automated. The reported cell death density was measured by averaging the TUNEL+ particle density on 3 near adjacent sections per animal from 3 animals of each genotype.

Ki67 and NeuroD1 quantification were done on Zeiss LSM 880 confocal images. Using ImageJ software,[96] Ki67-DAPI double positive or NeuroD1-Dapi double positive pixels were quantified and normalized to all DAPI positive pixels as a percentage. For every sample (n=3 per genotype), 3 sections and 6 40x images (212.55 X 212.55 μm) per section were quantified. On the graph, every point represents the averages of the 3 sections (18 images).

Images of EdU staining in the lateral posterior hemispheres of 3 near adjacent sections of the cerebellum of P12 animals were taken at 20x on a DM6000 Leica Microscope and processed using ImageJ Fiji Software.[96] Slides were stained with Sulfo-Cyanine5 azide (Lumiprobe Corporation, A3330) and Hoechst. The area of the EGL (mm^2) was measured manually and the number of EdU+ GCPs in the area between the paramedian and copula pyramis lobules were quantified using automation with ImageJ[96] and cell density reported. The reported density of EdU+ cells was measured by averaging the EdU+ cells on 3 near adjacent sections per animal from 3 animals of each genotype.

Quantification of CB and Tumor area

The area of the CB (mm2) and the Folding Index ((1-[convex length/EGL length]) x 100) at E18.5 in the *Nestin-Cre Kmt2d* mutants were measured manually on NanoZoomer digitized images of sections stained with H&E and measured using the NDP.view2 software from 3 sections per animal in 3 animals for each genotype.

The areas of the EGL/lesions at P12 and P21 were calculated as a percentage of the total area of the cerebellum. The regions were outlined manually on NanoZoomer digitized images of sections stained with H&E and area measured using the NDP.view2 software from 3 sections per animal in 3 animals for each genotype.

The areas of the metastatic tumors were calculated as a percentage of the total spinal cord area along the spinal cord. Sections were stained with GFP and DAPI and NanoZoomer digitized images created. NDP.view2 software was used to outline and measure the area of the tumors and the area of the spinal cord plus tumor on a serial series of coronal sections (every 10^{th} section; ~30 sections/mouse). The number of animals per genotype are listed in the Figures.

Transcriptome analysis

RNA sequencing reads were 3′ trimmed for base quality 15 and adapter sequences using version 0.4.5 of TrimGalore (https://www.bioinformatics.babraham.ac.uk/projects/trim_galore), and then aligned to mouse assembly mm10 with STAR v2.4 using default parameters. Data quality and transcript coverage were assessed using the Picard tool CollectRNASeqMetrics (http://broadinstitute.github.io/picard/). Read count tables were generated with HTSeq v0.9.1. Normalization and expression dynamics were evaluated with DESeq2[97] using the default parameters and the Wald test and outliers were assessed by sample grouping in principal component analysis. Gene set enrichment analysis (GSEA, http://software.broadinstitute.org/gsea) was run against MsigDB v6 using the pre-ranked option and log2 fold change for pairwise comparisons. Over-representation analysis was done in R using enrichGO in the clusterProfiler package. Network analysis was performed using enrichplot::cnetplot in R with default parameters. GEO ID: GSE211030.

Epigenome analysis

ATAC sequencing reads were trimmed and filtered for quality and adapter content using version 0.4.5 of TrimGalore (https://www.bioinformatics.babraham.ac.uk/projects/trim_galore), with a quality setting of 15, and running version 1.15 of cutadapt and version 0.11.5 of FastQC. Reads were aligned to mouse assembly mm10 with version 2.3.4.1 of bowtie2 (http://bowtie-bio.sourceforge.net/bowtie2/index.shtml) and were deduplicated using MarkDuplicates in version 2.16.0 of Picard Tools. To ascertain regions of chromatin accessibility, MACS2[98] (https://github.com/taoliu/MACS) was used with a p-value setting of 0.001. The BEDTools suite (http://bedtools.readthedocs.io)[99] was used to create normalized read density profiles. A global peak atlas was created by first removing blacklisted regions (http://mitra.stanford.edu/kundaje/akundaje/release/blacklists/mm10mouse/mm10.blacklist.bed.gz) then taking 500 bp windows around peak summits for ATAC and counting reads with version 1.6.1 of featureCounts (http://subread.sourceforge.net). DESeq2[97] was used to normalize read density (median ratio method) and to calculate differential enrichment for all pairwise contrasts. Peak-gene associations were created by assigning all intragenic peaks to that gene, and otherwise using linear genomic distance to transcription start site. Peak intersections were calculated using bedtools[99] v2.29.1 and intersectBed with 1 bp overlap. Gene set enrichment analysis (GSEA, http://software.broadinstitute.org/gsea) was performed with the pre-ranked option and default parameters, where each gene was assigned the single peak with the largest (in magnitude) log2 fold change associated with it. Motif signatures were obtained using Homer v4.5 (http://homer.ucsd.edu).[100] Composite and

tornado plots were created using deepTools v3.3.0[101] by running computeMatrix and plotHeatmap on normalized bigwigs with average signal sampled in 25 bp windows and flanking region defined by the surrounding 3 kb. Over-representation analysis was done in R using enrichGO in the clusterProfiler package (Table S6). Network analysis was performed using the output from clusterProfiler with enrichplot::cnetplot in R with default parameters. The RNA-ATAC scatterplot was created using peak-gene assignments described above. GEO ID: GSE211030.

Statistical analysis

All statistical analyses of quantified data from sections were performed using Prism software (GraphPad) and significance was determined as $P <= 0.05$. The statistical analysis used for each figure/subfigure is described in the figure legends.